

Mapping the merging zone of late infall in the AB Aur planet-forming system

JESSICA SPEEDIE ¹, RUOBING DONG ^{1,2}, RICHARD TEAGUE ³, DOMINIQUE SEGURA-COX ^{4,5}, JAIME E. PINEDA ⁶,
JOSH CALCINO ⁷, CRISTIANO LONGARINI ⁸, CASSANDRA HALL ^{9,10}, YA-WEN TANG ¹¹, JUN HASHIMOTO ^{12,13,14},
TERESA PANEQUE-CARREÑO ^{15,16}, GIUSEPPE LODATO ¹⁷ AND BENNEDETTA VERONESI ¹⁸

¹*Department of Physics & Astronomy, University of Victoria, Victoria, BC, V8P 5C2, Canada*

²*Kavli Institute for Astronomy and Astrophysics, Peking University, Beijing 100871, People's Republic of China; rbdong@pku.edu.cn*

³*Department of Earth, Atmospheric, and Planetary Sciences, Massachusetts Institute of Technology, Cambridge, MA 02139, USA*

⁴*Department of Astronomy, The University of Texas at Austin, 2500 Speedway, Austin, TX 78712, USA*

⁵*Department of Physics and Astronomy, University of Rochester, Rochester, NY 14627-0171, US*

⁶*Max Planck Institute for Extraterrestrial Physics, Gießenbachstraße 1, 85748, Garching bei München, Germany*

⁷*Department of Astronomy, Tsinghua University, 30 Shuangqing Rd, 100084 Beijing, China*

⁸*Institute of Astronomy, University of Cambridge, Madingley Road, Cambridge, CB3 0HA, United Kingdom*

⁹*Department of Physics and Astronomy, The University of Georgia, Athens, GA 30602, USA*

¹⁰*Center for Simulational Physics, The University of Georgia, Athens, GA 30602, USA*

¹¹*Academia Sinica, Institute of Astronomy and Astrophysics, 11F of AS/NTU Astronomy-Mathematics Building, No.1, Sec. 4, Roosevelt Rd., Taipei, Taiwan*

¹²*Astrobiology Center, National Institutes of Natural Sciences, 2-21-1 Osawa, Mitaka, Tokyo 181-8588, Japan*

¹³*Subaru Telescope, National Astronomical Observatory of Japan, Mitaka, Tokyo 181-8588, Japan*

¹⁴*Department of Astronomy, School of Science, Graduate University for Advanced Studies (SOKENDAI), Mitaka, Tokyo 181-8588, Japan*

¹⁵*Leiden Observatory, Leiden University, P.O. Box 9513, NL-2300 RA Leiden, the Netherlands*

¹⁶*European Southern Observatory, Karl-Schwarzschild-Str 2, 85748 Garching, Germany*

¹⁷*Università degli Studi di Milano, Via Celoria 16, 20133, Milano, Italy*

¹⁸*Univ Lyon, Univ Lyon1, Ens de Lyon, CNRS, Centre de Recherche Astrophysique de Lyon UMR5574, F-69230, Saint-Genis,-Laval, France*

ABSTRACT

Late infall events challenge the traditional view that planet formation occurs without external influence. Here we present deep ALMA $^{12}\text{CO } J = 2 - 1$ and $\text{SO } J_N = 5_6 - 4_5$ observations toward AB Aurigae, a Class II disk system with strong signs of gravitational instability and ongoing planet formation. By applying Keplerian and anti-Keplerian masks, we separate disk-like and non-disk-like motions of ^{12}CO , considering the two outputs as the ‘disk’ and ‘exo-disk’ (out of disk) emission components, respectively. The disk component of ^{12}CO extends to ~ 1600 au in radius and exhibits a stunningly rich architecture of global spiral structure. The exo-disk emission consists predominantly of three spiral structures –S1, S2 and S3– whose projections are co-spatial with the disk. We successfully reproduce their trajectories with a ballistic accretion flow model, finding that S1 and S2 (both redshifted) are infalling toward the disk from in front, and S3 (blueshifted) is infalling from behind. Where the terminal ends of S1 and S2 become indistinguishable from the disk, we observe a brightness peak in SO emission $2.5\times$ the azimuthal average of a background SO ring. This merging zone lies within a relatively confined region $15^\circ - 100^\circ$ east of north, and between $\sim 150 - 300$ au from the star, at scales relevant to where planet candidates have been previously identified. The AB Aur system provides a unified picture of late infall inducing replenishment of the disk, triggering gravitational instability, and modifying the conditions of forming planets.

Keywords: Protoplanetary disks(1300) — Planet formation(1241) — Gravitational instability(668)

1. INTRODUCTION

Recent scattered light and molecular observations are revealing more and more instances of large-scale narrow accretion filaments –‘streamers’– delivering material to circumstellar disks, a process referred to as ‘late-stage infall’ in the case of Class II disks (e.g., Ginski et al. 2021; Huang et al. 2021; Garufi et al. 2022; Harada et al. 2023; Pineda et al. 2023; Huang et al. 2024; Gupta et al. 2024). Modeling studies have shown that infalling material can have radical consequences for the disk chemistry and structure, including localized shock heating, the formation of pressure bumps, vortices or spiral arms, and disk warps or misalignments (e.g., Hennebelle et al. 2017; van Gelder et al. 2021; Kuffmeier et al. 2021; Kuznetsova et al. 2022; Calcino et al. 2024). Late infall in older Class II disks undergoing planet formation is thus highly relevant to the local conditions of forming planets.

AB Aurigae (AB Aur) is a 3.9 - 4.4 Myr old (DeWarf et al. 2003; Beck & Bary 2019; Garufi et al. 2024) Class II young stellar object (YSO; Henning et al. 1998; Bouwman et al. 2000) at a distance of 155.9 ± 0.9 pc (Gaia Collaboration et al. 2023). Several candidate protoplanets have been identified or predicted amongst the disk’s spiral arms (Dong et al. 2016; Tang et al. 2017; Boccaletti et al. 2020; Currie et al. 2022; Zhou et al. 2022; Biddle et al. 2024; Currie 2024), suggesting planet formation is underway. Optical and (sub)mm observations of the local environment have led numerous studies to propose that the AB Aur system is currently experiencing infall from its surroundings (Nakajima & Golimowski 1995; Grady et al. 1999; Tang et al. 2012; Dullemond et al. 2019; Rivière-Marichalar et al. 2020; Kuffmeier et al. 2020; Gupta et al. 2023). The disk itself has long been suspected to be gravitationally unstable (Fukagawa et al. 2004), and recently found to exhibit the predicted kinematic markers of gravitational instability (Hall et al. 2020; Longarini et al. 2021) in observations of ^{13}CO and C^{18}O emission with the Atacama Large Millimeter/submillimeter Array (ALMA; Speedie et al. 2024).

In this letter, we use high spectral resolution ALMA observations of $^{12}\text{CO } J = 2 - 1$ and $\text{SO } J_N = 5_6 - 4_5$ emission to investigate the hypothesis that late infall is inciting gravitational instability (GI) in this relatively evolved system. Unlike other systems fed by single-streamers observed on spatial scales that dwarf their end destination (e.g., Pineda et al. 2020; Valdivia-Mena et al. 2022, 2023; Flores et al. 2023; Cacciapuoti et al. 2024; Gupta et al. 2024), the AB Aur system hosts *multiple* ‘out-of-plane’ spiral arms *on disk scales*, detected in previous ^{12}CO observations (Tang et al. 2012). In the 2D sky plane, these structures appear co-spatial with

the disk, necessitating new techniques for isolating their emission and presenting a unique opportunity to study the interface between the disk and infalling material in detail.

2. OBSERVATIONS

We observed AB Aur with ALMA in Cycle 8 under program ID 2021.1.00690.S (PI: R. Dong). Here we present the $^{12}\text{CO } J = 2 - 1$ ($\nu_{\text{rest}} = 230.538$ GHz, $E_{\text{up}} = 16.6$ K) and $\text{SO } J_N = 5_6 - 4_5$ ($\nu_{\text{rest}} = 219.949$ GHz, $E_{\text{up}} = 35.0$ K) molecular emission line components from this program, which were reduced and imaged concurrently with the $^{13}\text{CO } J = 2 - 1$ and $\text{C}^{18}\text{O } J = 2 - 1$ components presented in Speedie et al. (2024). We refer the reader to that work for data processing details, and briefly reproduce the key aspects below¹.

2.1. Calibration

Measurements were taken in a short-baseline configuration C-3 (2 execution blocks) and a long-baseline configuration C-6 (6 execution blocks), using the Band 6 receivers (Ediss et al. 2004). We configured two spectral windows to target the $^{12}\text{CO } J = 2 - 1$ and $\text{SO } J_N = 5_6 - 4_5$ lines, and dedicated a single 2.0 GHz spectral window to sampling the continuum, centered at 233.012 GHz. Using the continuum data, we aligned the eight execution blocks to a common phase center in the uv -plane (employing the EXOALMA alignment script; Loomis et al. submitted). Manual self-calibration was first performed on the short-baseline continuum data, starting with 6 rounds of phase-only calibration down to a solution interval of 18 s, followed by 1 round of amplitude+phase calibration on the interval of a scan length, resulting in a SNR increase by a factor of 2.2. Self-calibration subsequently continued on the concatenated short- and long-baseline continuum data, undergoing 4 rounds of phase-only calibration down to 60 s followed by 1 round of amplitude+phase calibration on the interval of a scan length, yielding a SNR increase by a factor of 1.5. Finally, the phase center shifts and self-calibration solutions acquired with the continuum data were applied to the line data, and continuum subtraction was done in the uv -plane.

2.2. Imaging

Imaging was undertaken with the CASA `tclean` task. The ^{12}CO data immediately presented two challenges: (i) the presence of large-scale diffuse emission with non-Keplerian morphologies, for which generating the optimal CLEAN mask became a protracted and nebulous

¹ An online guide to the reduction and imaging for the full program is available at <https://jjspeedie.github.io/guide.2021.1.00690.S>

Table 1. Molecular lines and properties of the imaged ALMA data cubes (program ID 2021.1.00690.S).

Transition	Rest Frequency (GHz)	Channel Width (m/s)	robust	Beam ("×", deg)	rms (mJy/beam)	JvM ϵ
$^{12}\text{CO } J = 2 - 1$	230.538	42.0	0.5	$0.23 \times 0.17, 0.2$	1.55	0.49
SO $J_N = 5_6 - 4_5$	219.949	84.0	1.5	$0.39 \times 0.28, 171.2$	0.63	0.34

goal; and (ii) the presence of negative bowling (Braun & Walterbos 1985; Holdaway 1999), particularly in central channels. Negative bowling, where the recovered (positive) emission appears to sit in a bowl of negative flux (e.g. Fig. 7 of Faridani et al. 2018), is a fundamental interferometer image artifact caused by the presence of emission on spatial scales larger than the reciprocal of the shortest measured baselines (known as the Maximum Recoverable Scale, MRS) and can only be solved by obtaining additional observations sampling the visibility function at smaller uv -spacings. Animated ^{12}CO channel maps illustrating the negative bowling are available (Figure 8) in the online article. The MRS of our short-baseline configuration, C-3, is $\sim 7''$ at 230 GHz (Remijan et al. 2019).

We adopted the following strategies in response to both of the above two issues: First, we cleaned with a broad mask² encompassing all emission within the field of view (FOV), and accordingly, we cleaned conservatively (to a threshold of $5\times$ the rms noise measured in 20 line-free channels of the dirty cube). Second, we forced frequent major cycles³ to repeatedly re-populate the uv -plane and interpolate into the missing short uv -spacings. These strategies borrowed from the philosophy of PHANGS-ALMA (Leroy et al. 2021). We used the multiscale deconvolution algorithm (Cornwell 2008) with Gaussian deconvolution scales [0.02'', 0.1'', 0.3'', 0.6'', 1.0''], with an additional largest scale of 2.0'' appended for ^{12}CO . We adopted a Briggs robust weighting scheme, and imaged in LSRK velocity channels at 42 m/s for ^{12}CO and 84 m/s for SO. Unless otherwise specified, the images presented in this work use `robust=0.5` for ^{12}CO and `robust=1.5` for SO, and are JvM corrected (Jorsater & van Moorsel 1995; Czekala et al. 2021) and primary beam corrected. Table 1 lists details for each image cube. The rms noise is measured within an annulus of 4'' inner radius and 8'' outer radius over the first and last 5 channels of the cube.

We used the `bettermoments` package (Teague & Foreman-Mackey 2018a,b) to generate maps of peak intensity, velocity-integrated intensity (moment 0), and intensity-weighted velocity (moment 1) throughout this

² We used the `tclean` arguments `usemask='pb'` and `pbmask=0.2`, which sets a cleaning mask extending to where the 12m antenna primary beam gain reaches the 20% level, which is usually considered the edge of the FOV.

³ The ^{12}CO cube with `robust=0.5` underwent 282 major cycles.

work. We applied σ -clipping at $5\times$ the rms noise for ^{12}CO and $3\times$ the rms noise for SO.

2.3. Overview with Standard Moment Maps

Figure 1 introduces our ALMA observations of the AB Aur disk. For scale, the VLT/SPHERE H -band scattered light image at 1.6 μm is shown in Figure 1a (Boccaletti et al. 2020; Speedie et al. 2024 reduction). Figure 1b presents our ALMA $^{12}\text{CO } J = 2 - 1$ integrated intensity map, collapsed uniformly over velocities ± 6 km/s about the systemic velocity ($v_{\text{sys}} = 5.85$ km/s; Tang et al. 2012; Speedie et al. 2024). We find that the disk extends to $r \sim 10''$ ($r \sim 1600$ au) in ^{12}CO emission, placing it among the largest protoplanetary disks known both physically and on the sky (e.g., Berghea et al. 2024; Monsch et al. 2024). Spiral structure at all radii and azimuth is visible directly in the integrated intensity map. The ratio of the disk emission extent ($\sim 20''$) to the synthesized ALMA beam ($\sim 0.2''$) is ~ 100 .

Figure 1c shows our SO $5_6 - 4_5$ peak intensity map, generated over a velocity range ± 2.5 km/s about v_{sys} . We observe a ring of SO emission between $r = 1.0'' - 2.0''$ on the sky. The ring exhibits substructure, namely a brightness peak in the northeast. Measuring the azimuthal extent of the brightness peak as the region where the peak intensity is above 10 mJy/beam (70% of the maximum), we find a position angle range of $32^\circ - 82^\circ$ east of north. The maximum SO intensity inside this region is 14.5 mJy/beam, which is a relative increase of 150% from the azimuthal average intensity of 5.7 mJy/beam measured throughout the rest of the ring. We confirmed that this brightness peak is not an artifact of continuum subtraction (see Figure 6 in Appendix A).

3. THE DISK AND EXO-DISK COMPONENTS OF ^{12}CO

In this section and §4, we present a position-velocity (PV) analysis of the $^{12}\text{CO } J = 2 - 1$ and SO $J_N = 5_6 - 4_5$ emission. We begin in §3.1 with radial PV diagrams to reveal the complexity in the ^{12}CO data. In §3.2 we kinematically disentangle the ^{12}CO into its disk-like and non-disk-like components, in preparation to model the latter component as infall in §4.

3.1. Radial Position-Velocity Diagrams

Figure 2 presents radial PV diagrams of $^{12}\text{CO } J = 2 - 1$ and SO $J_N = 5_6 - 4_5$ emission extracted along the disk's major and minor axes. The SO is plotted over

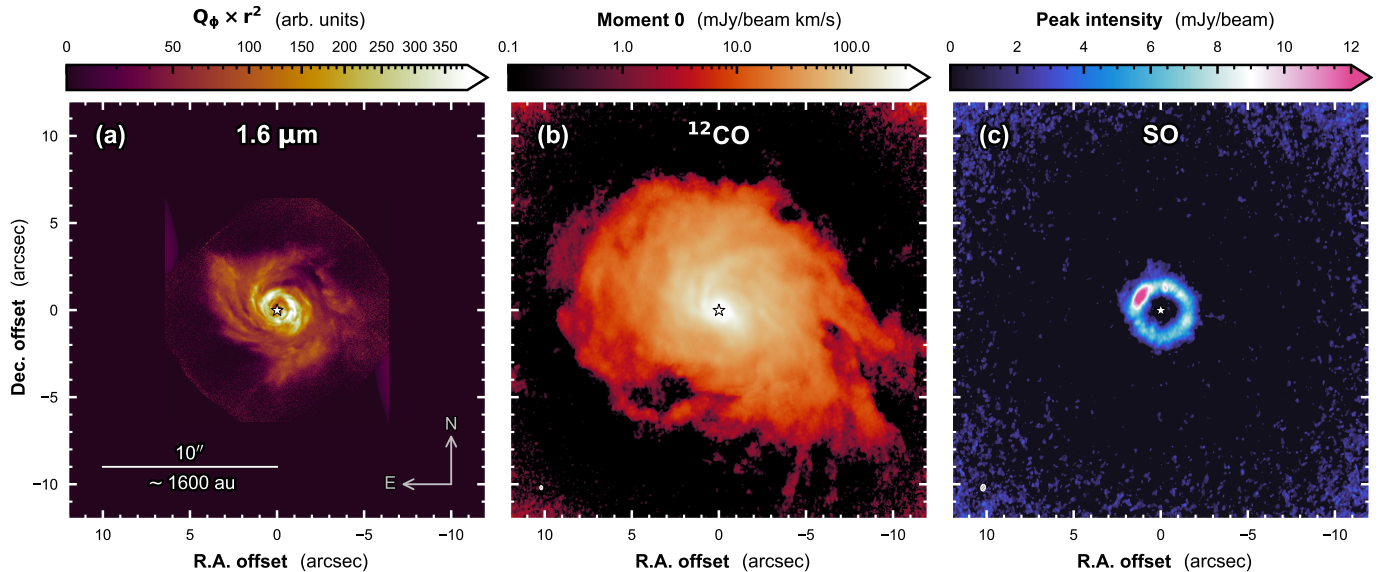


Figure 1. Introducing our ALMA observations. (a) VLT/SPHERE H -band scattered light image at $1.6 \mu\text{m}$ (Boccaletti et al. 2020), shown for scale. (b) ALMA $^{12}\text{CO } J = 2 - 1$ integrated intensity map, collapsed uniformly over line-of-sight velocities $\pm 6 \text{ km/s}$ about v_{sys} . Emission extends $\sim 20''$ ($\sim 3200 \text{ au}$) in diameter, roughly half the diameter of the 12m-antenna field of view in Band 6. (c) ALMA SO $J_N = 5_6 - 4_5$ peak intensity map. The ring takes a brightness peak in the northeast.

the ^{12}CO as filled contours. The PV slices are taken assuming a geometrically thin disk with inclination $i = 23.2^\circ$ (from the continuum; Tang et al. 2012, 2017) and position angle P.A. = 236.7° (where P.A. is measured east of north to the redshifted major axis; Speedie et al. 2024). We used `pvextractor` (Robitaille et al. 2018) for all PV slicing throughout this work.

Along the major axis (top row of Figure 2), the projection of the disk’s rotation is maximized, and we observe substantial excess ^{12}CO emission cleanly distinct in velocity from the bulk rotating component. For comparison, we overlay dashed orange curves of Keplerian rotation in a razor thin disk, following $v_{\text{LOS}} - v_{\text{sys}} = v_{\text{Kep}} \sin i \cos \phi$, where $v_{\text{Kep}} = (GM_*/r)^{1/2}$, the stellar mass $M_* = 2.23 M_\odot$, the systemic velocity $v_{\text{sys}} = 5.86 \text{ km/s}$ (Speedie et al. 2024), and $\cos \phi = 1$ on the redshifted major axis.

Three strong ‘blobs’ are identifiable within the excess ^{12}CO emission in the top row of Figure 2 (labeled S1 to S3). They correspond to radial cross sections through three ‘out-of-plane’ spiral structures first identified by Tang et al. (2012) in $^{12}\text{CO } J = 2 - 1$ observations with the Plateau de Bure interferometer (PdBI). Following Tang et al. (2012), we hereafter refer to them as S1, S2, and S3. They have additionally been observed in the same transition with NOEMA by Rivière-Marichalar et al. (2020). To our knowledge, we present the first ALMA detection.

Note that the Keplerian rotation curves do not account for the disk’s contribution to the gravitational potential. The disk component of ^{12}CO emission shows substantial apparent super-Keplerian rotation at large radii in the major axis PV diagrams, indicative of sig-

nificant self-gravity and a high disk-to-star mass ratio. We keep to qualitative statements here because these major axis slices were taken along a straight line, which is equivalent to assuming the ^{12}CO emission surface is the disk midplane. For now we note that the surface is almost certainly elevated, and thus the slices are likely sampling slightly away from the loci of v_{LOS} maxima. A quantitative kinematic analysis to fit for the disk mass should be done (e.g. Veronesi et al. 2021; Lodato et al. 2023; Martire et al. 2024; Andrews et al. 2024), though complexities in the ^{12}CO emission, the non-axisymmetric nature of the disk and its low inclination complicate the extraction of a ^{12}CO emission layer. We tender that challenge to future work.

Along the minor axis (bottom row of Figure 2), we notice how the ^{12}CO emission appears to bifurcate (or fork) into two bands above and below the horizontal line of $v_{\text{LOS}} - v_{\text{sys}} = 0$ at large offsets, starting around $r \gtrsim 3.5''$. We understand this to be a result of interferometric spatial filtering in the central channels (§2).

3.2. Keplerian & Anti-Keplerian Masking

Next, we disentangle the bulk rotating component of ^{12}CO emission from all its non-disk-like emission, in a fashion similar to Huang et al. (2021, see their Appendix C). We generate a Keplerian mask (Teague 2020) to kinematically encompass the disk, and an ‘anti-Keplerian’ mask with opposite Boolean values to encompass any emission kinematically inconsistent with the disk. We additionally spectrally smooth each mask, i.e., convolve the top hat spectrum in each spatial pixel with a Gaussian, to mitigate edge artifacts (c.f. Figure 17 of Huang et al. 2021), which also introduces some

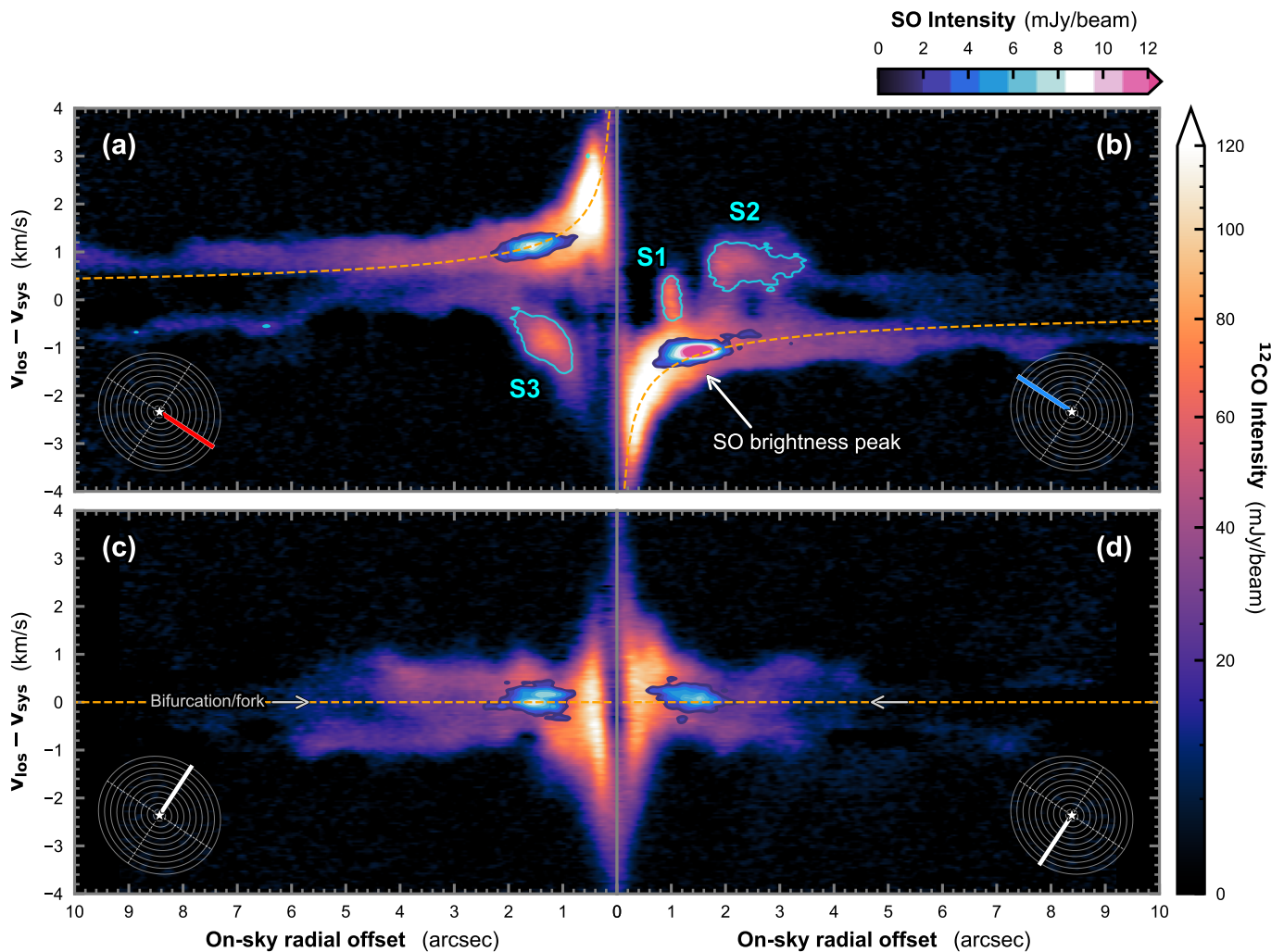


Figure 2. Position-velocity (PV) slices in ALMA $^{12}\text{CO } J = 2 - 1$ emission along the disk major and minor axes. PV slices in the ALMA SO $J_N = 5_6 - 4_5$ emission are overplotted as filled contours in increments of 2σ starting at 3σ , where $\sigma = 0.63$ mJy/beam. The orientation of each slice is indicated in the bottom corner of each panel: (a) Redshifted (west) major axis. (b) Blueshifted (east) major axis. (c) Northern minor axis. (d) Southern minor axis. Keplerian rotation is denoted by orange dashed lines, accounting for the mass of the central star only. ‘Out-of-plane’ spiral arms S1, S2 and S3 identified by Tang et al. (2012) are labeled, and encircled by cyan contours from the anti-Keplerian weighted ^{12}CO cube (see next figures). In panels (c) and (d), grey arrows point to a bifurcation pattern we attribute to interferometric filtering (§2). An animation of radial position-velocity slices in ALMA $^{12}\text{CO } J = 2 - 1$ and SO $J_N = 5_6 - 4_5$ emission is available in the online Journal. The animation sequence pans through all azimuthal angles in 0.5° steps following the rotation direction of the disk.

overlap in their spectra. Two new versions of the $^{12}\text{CO } J = 2 - 1$ ALMA image cube are then generated by multiplication with each of the Keplerian and anti-Keplerian masks. In this way, the masks serve effectively as 3D weighting functions. Further details are provided in Appendix B and Figure 7. In the remainder of this letter, we refer to the emission in the Keplerian-weighted and anti-Keplerian-weighted ^{12}CO cubes as the “disk” and “exo-disk”⁴ components, respectively.

⁴ As in ‘outside of disk’, in the same sense as ‘exo-terrestrial’ or ‘exo-solar planet’.

Figure 3 shows moment maps collapsed from the Keplerian and anti-Keplerian $^{12}\text{CO } J = 2 - 1$ image cubes. We emphasize that the masking process is not perfect, but is meaningfully effective considering the complexity of the ^{12}CO emission (Fig. 2). Beginning with the left column, Figure 3a shows the integrated intensity map of the map of the Keplerian-weighted ^{12}CO , or disk component. The inset panel shows the corresponding intensity-weighted velocity map, demonstrating that the emission isolated by the Keplerian mask is at least broadly recognizable as disk-like, with a redshifted and blueshifted side (compare to Figure 3 of Rivière-Marichalar et al. 2020). Figure 3c shows a high-pass filtered version of

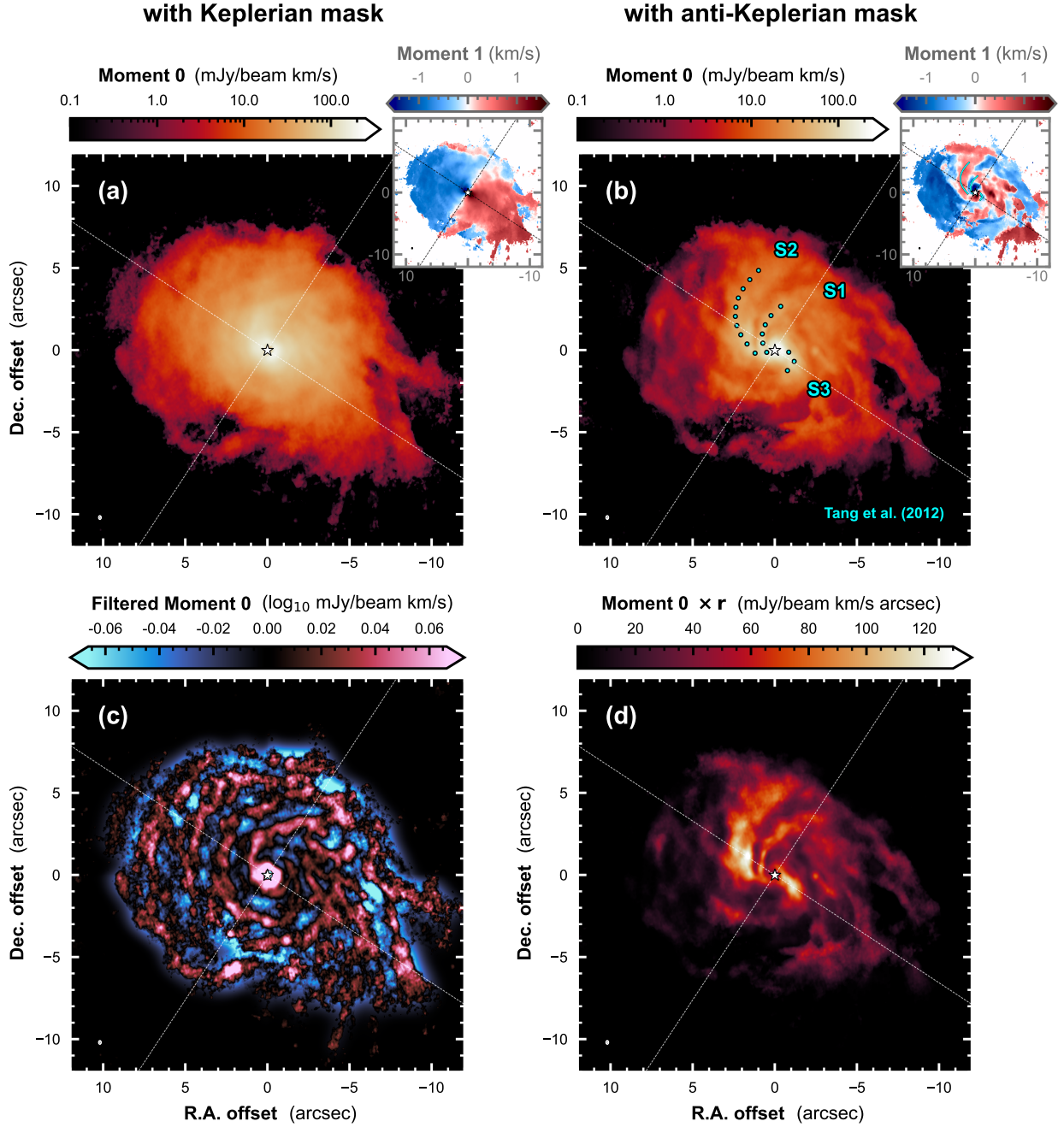


Figure 3. ALMA $^{12}\text{CO } J=2-1$ moment maps after disentangling the disk and exo-disk emission. (a) Integrated intensity map of ^{12}CO after weighting with a spectrally-smoothed Keplerian mask. (b) The same, but after weighting with an anti-Keplerian mask generated with opposite Boolean values prior to spectral smoothing. Views of the masks are provided in Appendix Figure 7. The cyan points trace S1, S2 and S3 from Table 4 of Tang et al. (2012). Panels (a) and (b) are shown on a \log_{10} colorscale to compare with Figure 1b. Intensity-weighted velocity maps are shown in the insets. (c) High-pass filtered integrated intensity map of the Keplerian-weighted ^{12}CO cube in panel (a), highlighting the architecture of spiral structure within the disk. (d) The same as panel (b), but scaled by r (on-sky) and presented on a linear colorscale.

Figure 3a, made with a radially expanding Gaussian kernel⁵ using the same parameter setting as Speedie et al. (2024). A rich architecture of spiral structure exists in the disk component, consistent with ongoing gravitational instability (e.g., Dipierro et al. 2014; Hall et al. 2019).

In the right column of Figure 3, we show moment maps of the anti-Keplerian-weighted ¹²CO cube, or exo-disk component. Figure 3b presents the integrated intensity map, where points along the spiral structures S1, S2, and S3 placed by Tang et al. (2012, their Table 4) are overplotted in cyan for reference. Figure 3d shows the integrated intensity map r -scaled with a linear colorbar. The exo-disk component is comprised predominantly of coherent spirals S1, S2 and S3, with additional ‘whisps’ of emission (particularly in the west and south). The corresponding intensity-weighted velocity map (Figure 3b inset) is markedly non-disk-like, with regions of emission at ‘opposite’ line-of-sight velocity to the disk.

We note that the imprint of S1 is visible in the *disk* component (compare Figure 3c and d). In other words, some of its emission remains within the Keplerian mask. As we’ll discuss in the next section, this is because emission from S1 is not sufficiently offset in line-of-sight velocity from the disk component *along its entire* trajectory (not just at the major axis as we glimpsed in Figure 2b). On the other hand, S2 and S3 are kinematically distinct from the disk at almost all their spanned azimuths.

4. MODELING THE EXO-DISK COMPONENT AS INFALL

We focus on the coherent exo-disk spiral structures S1, S2, and S3, and show that their trajectories (in both RA-Dec and PV space) can be reproduced with the analytic accretion flow model of Mendoza et al. (2009), using the numerical implementation by Pineda et al. (2020). Interpreting the exo-disk emission as infall is well motivated: observations of AB Aur’s kilo-au environment are highly suggestive of interaction with surrounding material (e.g., Grady et al. 1999). See more details in Figure 8 of Appendix C. The next subsection outlines the scheme of the model, with our results presented in §4.2.

4.1. The Pineda Implementation of the Mendoza Streamline Model (PIMS)

The Mendoza et al. (2009) model considers a steady-state ballistic accretion flow from a rigidly rotating sphere of finite radius r_0 (representing the inner edge of a giant molecular cloud) toward a central object with mass M , located at the origin of coordinates. The angular frequency of the sphere’s rigid-body rotation is Ω . In spherical coordinates, a fluid ‘particle’ is initiated on

the sphere at an azimuthal angle ϕ_0 and a polar angle θ_0 (where $\theta = 90^\circ$ defines the equatorial plane). It can also be given an initial radial velocity, $v_{r,0}$. The particle has specific angular momentum h about the origin inherited from its initial location, where h is distributed on the sphere according to $h = h_0 \sin \theta$ assuming $h_0 = r_0^2 \Omega$. The particle’s specific energy E is the sum of its specific kinetic energy, centrifugal potential energy, and gravitational potential energy:

$$E = \frac{1}{2}v_r^2 + \frac{1}{2}\frac{h^2}{r^2} - \frac{GM}{r} = \frac{1}{2}v_{r,0}^2 + \frac{1}{2}\frac{h_0^2 \sin^2 \theta_0}{r_0^2} - \frac{GM}{r_0}. \quad (1)$$

The quantities h and E are constants of motion along each particular trajectory.

The trajectory of each particle (hereafter a ‘streamline’) is a solution to Kepler’s problem (Newton 1687), and therefore a segment of a conic section with the origin at one of the foci. This means each streamline is contained in a plane, and we will later refer to this as the plane ‘of’ a streamline. The whole system is cylindrically symmetric, such that each streamline ‘collides’ with its reflection counterpart at the equatorial plane. An important fundamental property of the model is that a streamline cannot spiral infinitely – it *must* hit the equatorial plane after traveling an azimuthal distance of $< 90^\circ$ from its initial azimuthal location ϕ_0 . It comes closest to subtending this maximum azimuthal distance when initialized close to the equatorial plane ($\cos(\phi - \phi_0) = \tan \theta_0 / \tan \theta$; Equation 8 of Mendoza et al. 2009).

With the Pineda et al. (2020) Implementation of the Mendoza et al. (2009) Streamline Model (PIMS⁶), we have 6-dimensional information – 3 spatial coordinates and 3 velocity coordinates – at every point along the streamline. Two rotational transformations are then applied to the coordinates to project the system onto the sky: a first to give the streamline’s equatorial plane some inclination, and a second to give the ascending node some position angle⁷. This yields 3D spatial coordinates (RA, Dec, LOS) and 3D velocity components $\langle v_{\text{RA}}, v_{\text{Dec}}, v_{\text{LOS}} \rangle$ at every point on the streamline. We further compute the projected radial coordinate, r_{proj} , as the hypotenuse of the RA and Dec coordinates. When we compare streamlines to the AB Aur data, we do so in the RA-Dec plane and the $r_{\text{proj}}-v_{\text{LOS}}$ (PV) plane.

We obtained streamline solutions for each of S1, S2 and S3 by first exploring their trajectories in radial and azimuthal PV cross sections to build an understanding of their v_{LOS} behaviour as a function of ϕ and r . A selection of such cross sections is shown in Figure 9 of Appendix D, with animated versions available in the online

⁶ github.com/jjspeedie/pims

⁷ We note that the line-of-sight velocity, v_{LOS} , is invariant under this transformation (v_{LOS} is independent of the position angle).

⁵ github.com/jjspeedie/expanding_kernel

article. We then identified, by manual experimentation, the region of model parameter space where streamlines follow a broadly similar track in the PV plane. This procedure leverages the fact that the infall model trajectories in the $r_{\text{proj}}-v_{\text{LOS}}$ plane only take one of a few basic shapes (e.g. see Thieme et al. 2022; Mori et al. 2024, for examples). From there, we iteratively fine-tuned the parameters until the match between the streamlines and the observed trajectories in the RA-Dec and PV planes were visually satisfactory. The only parameter we did not let vary in these experiments is M , which we set to $M = 2.90 M_{\odot} = M_{\star} \times 130\%$ to represent both the central star and the disk (Speedie et al. 2024).

In the following subsection, we present one streamline solution for each of S1, S2 and S3. The PIMS parameters describing streamlines are provided in Table 3 of Appendix E. We note that for each of S1 and S2, our procedure easily yielded a family of streamlines that are satisfactory matches. We confirmed each family describes a structure physically coherent in 3D spatial coordinates, $(\text{RA}, \text{Dec}, \text{LOS})$ (see Figure 10 in Appendix E), and selected one solution to show in the main text. Satisfactory solutions for S3, on the other hand, were not so easily found; we nonetheless present our single best solution for S3 for discussion and for reference with Tang et al. (2012).

4.2. Streamline Solutions for S1, S2 and S3

Figure 4 presents our infall modeling results for each of S1, S2 and S3. In Figure 4a, we overlay the three PIMS streamline RA-Dec trajectories onto the ^{12}CO anti-Keplerian moment 1 map (from Figure 3b inset). The streamlines fall from large radii to small radii, and are coloured by their line-of-sight velocity, v_{LOS} . The S1 and S2 streamlines are predominantly redshifted (where the AB Aur disk is blueshifted) and lie in front of the disk, falling toward the disk away from us. The plane of S1 is approximately 20° inclined with respect to the AB Aur disk midplane, and the plane of S2 is inclined by approximately 35° . S3 is blueshifted (where the disk is redshifted) and lies behind the disk, falling toward us, on a plane inclined by approximately 45° to the AB Aur disk midplane. See Figure 10 for a 3D rendering and animation of the system geometry.

In Figure 4bcd, we overlay each of the streamline $r_{\text{proj}}-v_{\text{LOS}}$ trajectories onto PV diagrams from the ^{12}CO image cube, where the PV slices were taken in the data cube along each of the streamlines’ RA-Dec trajectories for completely consistent comparison (see Figure 9 of Huang et al. 2021, for another example of this). To help visually discern the disk and exo-disk components of the ^{12}CO emission in this space, the same slices were taken through each of the Keplerian- and anti-Keplerian weighted ^{12}CO image cubes, and overplotted with orange and cyan contours, respectively. Finally, we take the same slices through the SO $J_N = 5_6 - 4_5$ cube, and

overplot the SO emission as filled contours as well (like Figure 2).

We find that both S1 and S2 –the observed structures– follow a ‘flatline-then-dip’ trajectory in the $r_{\text{proj}}-v_{\text{LOS}}$ plane as they accelerate toward the star. We identify the ‘merging zone’ of S1 and S2 as the region where their emission in ^{12}CO becomes indistinguishable from the emission from the disk, which is also where the terminal ends of our model streamlines intersect with the disk midplane in 3D spatial coordinates (Figure 10). Figure 4b and d show this from the perspective of PV slices along the streamlines themselves, and Appendix Figure 9 shows this from the perspective of PV slices in radius and azimuth. The merging occurs at radii $r \sim 1'' - 2''$ from the star and between position angles $15^\circ - 100^\circ$ east of north on the sky. SO $J_N = 5_6 - 4_5$ emission is observed at these same radii, peaking within this position angle range (§2.3), and at line-of-sight velocities consistent with Keplerian, indicating localized heating within the disk (discussed further in §5.3).

We note that, as mentioned in §3.2, emission from S1 is not well separated in line-of-sight velocity from the disk component along its entire trajectory (see Figure 4b), while emission from S2 is kinematically distinct from the disk at all its spanned azimuths leading up to the merging zone (Figure 4d). This can be explained as a projection effect: Both are observed at redshifted line-of-sight velocities within roughly $0 - 1$ km/s above v_{sys} , but S1 is spatially nearer to the minor axis (particularly at large radii), where the disk emission already occupies these line-of-sight velocities. Away from the minor axis (looking east), rotation projects the disk blueward of v_{sys} , such that emission from S2 is separated in line-of-sight velocity over the course of its approach.

Turning to Figure 4c, S3 is observed in ^{12}CO at blueshifted line-of-sight velocities within roughly $0 - 2$ km/s below v_{sys} . Lying spatially near the western major axis, it is well separated from the disk’s redshifted emission. We found that the analytic infall model cannot produce a streamline that simultaneously (i) is blueshifted, (ii) is located on the redshifted side of the disk, (iii) is oriented in a counter-clockwise sense on the sky, and (iv) takes a concave-down trajectory in the $r_{\text{proj}}-v_{\text{LOS}}$ plane. We present a streamline that violates solely attribute (iv). The terminal end of the model streamline lies on the redshifted major axis at $r \sim 0.5''$, both spatially and kinematically offset from the observed SO emission.

5. DISCUSSION

Figure 5 provides a summary of our main result. We have applied a simple ballistic accretion flow model (used by previous works to analyze streamers on cloud or envelope scales, e.g., Pineda et al. 2020; Valdivia-Mena et al. 2022; Garufi et al. 2022; Valdivia-Mena et al. 2023; Flores et al. 2023) onto *disk-scales*, in a system with multiple infalling disk-scale streamers and several em-

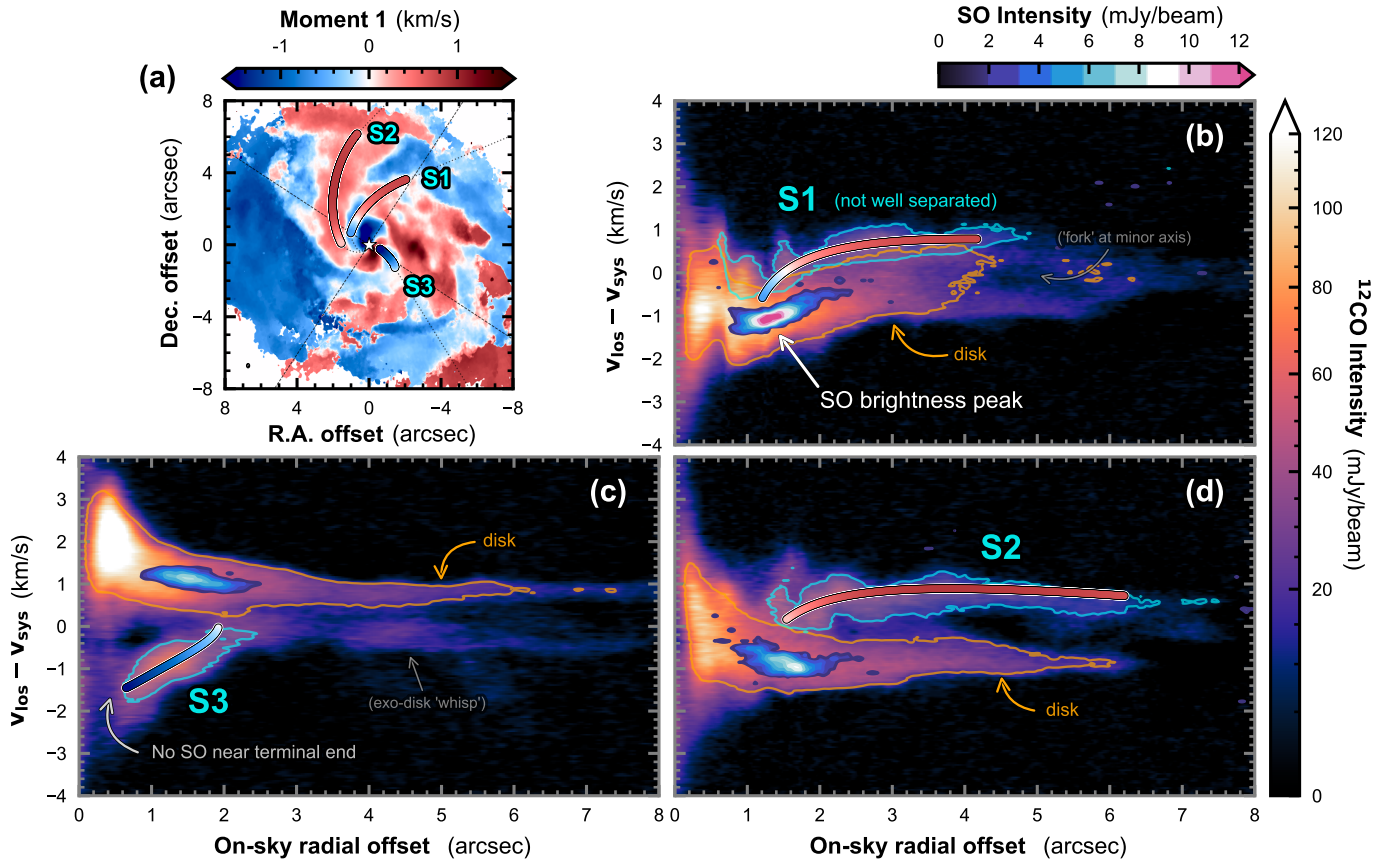


Figure 4. Modeling S1, S2 and S3 as infall. (a) Intensity-weighted velocity map of the anti-Keplerian weighted ^{12}CO $J = 2 - 1$ image cube (as in Figure 3b inset). We overlay RA-Dec trajectories of three streamlines matching S1, S2 and S3, computed with the analytic accretion flow model of Mendoza et al. (2009) implemented in (Pineda et al. 2020). The colorbar for velocity applies to both the background velocity map and the model streamlines. (b,c,d) PV slices taken *along the RA-Dec trajectory* of each streamline for completely consistent comparison between model and data (one panel per streamline). Within a panel, multiple cubes have been sliced: the full unweighted ^{12}CO cube (colormap), the Keplerian weighted ^{12}CO cube (orange contours), and the anti-Keplerian weighted ^{12}CO cube (cyan contours). PV slices in the SO $J_N = 5_6 - 4_5$ image cube are overplotted as filled contours in increments of 2σ starting at 3σ . We concatenate arbitrary extensions to the slice paths so that the PV diagrams span $r = 0'' - 8''$ in on-sky radial offset, shown as dotted gray lines extending from both ends of the streamline trajectories. Radial and azimuthal PV cross sections providing additional visualizations of S1 and S2 merging with the disk are available in Appendix Figure 9.

bedded planet candidates. Figure 5c shows that S1 and S2 are seen in $0.57 \mu\text{m}$ HST/STIS imaging (Grady et al. 1999), consistent with being in front of the disk. We identify the ‘merging zone’ of S1 and S2 as the region where their emission in ^{12}CO becomes indistinguishable from the emission from the disk (Figure 4 & 9), which is also where our model streamlines intersect with the disk midplane in 3D spatial coordinates (Figure 10). In this same region, we observe a brightness peak in SO $J_N = 5_6 - 4_5$ emission. We highlight that the merging zone is in close proximity to candidate sites of planet formation.

5.1. What are the origins of late infall in the AB Aur system?

Late-stage infall events may be the result of low-velocity cloud fragments being gravitationally captured by the star, and accreted through a Bondi-Hoyle Lyttleton (BHL) type process (Bondi 1952; Edgar 2004). Zooming out to AB Aur’s kilo-au environment, optical images with the University of Hawaii 2.2 m Telescope show an arc-shaped structure or “reflection nebula” surrounding AB Aur from the east to the south (Grady et al. 1999; Nakajima & Golimowski 1995). This arc structure is hypothesized to be part of a cloudlet unrelated to the early protostellar collapse phase – specifically, a part that was *not* captured by the gravity of AB Aur, and instead was bent during a flyby encounter onto an arc-shaped (hyperbolic) trajectory (Dullemond et al. 2019; Kuffmeier et al. 2020; Gupta et al. 2023). Such a scenario, but playing out around DG Tau, was

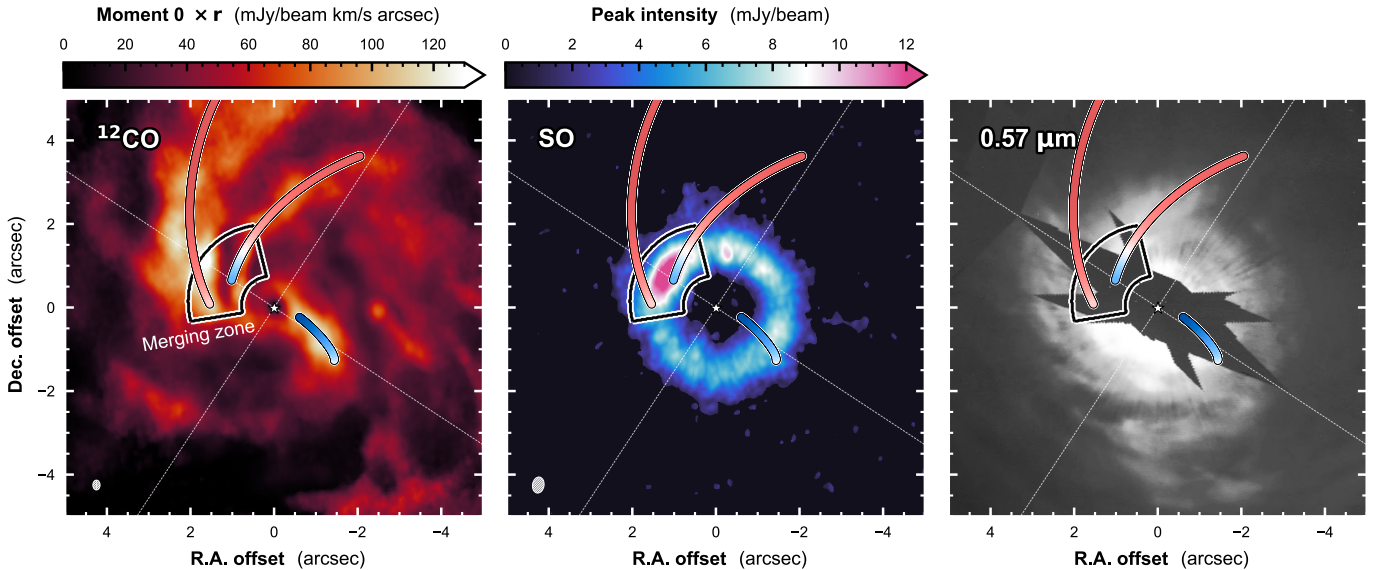


Figure 5. The merging zone of late infall in the AB Aur disk. The streamline trajectories for S1, S2 and S3 from Figure 4 are overlaid onto the exo-disk $^{12}\text{CO } J = 2 - 1$ integrated intensity map (as in Figure 3d), the SO $J_N = 5_6 - 4_5$ peak intensity map (as in Figure 1c) and HST/STIS scattered light image at $\lambda = 0.57 \mu\text{m}$ (Figure 3 of Grady et al. 1999, reproduced with permission). The terminal ends of S1 and S2 coincide with the SO $J_N = 5_6 - 4_5$ brightness peak. A rendering of the disk+streamline geometry in 3-dimensional space is available in Appendix Figure 10.

recently demonstrated with hydrodynamic simulations by Hanawa et al. (2024).

In Figure 8 (Appendix C) we report new but very tentative evidence supporting this hypothesis in AB Aur. The closest projected separation of the reflection nebula, ~ 1500 au or $\sim 10''$, falls within the field of view of our ALMA observations ($38'' \times 38''$). In ^{12}CO emission, we observe a faint ‘tail-like’ emission structure extending from the disk to the south, bridging the disk to a source outside the primary beam FOV. The tail appears copatial with the reflection nebula on the sky, hinting to a physical connection and suggesting that some part of the cloudlet has been gravitationally captured. Further notes on the tail structure are provided in Appendix C. We stress this detection is tentative as the relative response of the ALMA 12m antenna sensitivity tapers to the 20% level at the edge of our imaged FOV (§2). Follow-up kinematic observations probing a larger region of sky and with sensitivity to those larger spatial scales are needed. The connection, if any, between the ‘tail-like’ emission at the southern edge of the FOV and the streamers observed *within* the confines of the disk –S1, S2 and S3– is unclear.

5.2. What are the consequences of late infall in the AB Aur system?

The consequences of infall are fundamental and wide-reaching (e.g., Kuffmeier et al. 2023; Pelkonen et al. 2024; Winter et al. 2024). In this section we focus our lens on angular momentum transport and disk substructure.

Material infalling into a pre-existing disk must trigger some form of angular momentum redistribution for the new mass to be ‘assimilated’ into the disk (e.g., Kratter & Lodato 2016). Numerical simulations have shown gravitational instabilities to be triggered and/or spiral structure to be formed as a consequence of infall (e.g., Harsono et al. 2011; Lesur et al. 2015; Hennebelle et al. 2017; Kuffmeier et al. 2018). Indeed, infall has been previously proposed to trigger GI in Elias 2-27 (Paneque-Carreño et al. 2021). In an evolved system like AB Aur, an influx of mass may have been necessary to acquire and maintain a high disk-to-star mass ratio (Fukagawa et al. 2004; Hall et al. 2019). If gravitationally unstable disks only exhibit prominent spiral structure for a limited time after the onset of GI, as suggested by recent numerical simulations (Rowther et al. 2024), then we may infer that gravitational instability must have been triggered –e.g. by infall– relatively recently.

In addition to gravitational instabilities, simulations have shown infall to launch the Rossby wave instability (RWI), resulting in the ready formation of vortices and pressure bumps where material is deposited (Bae et al. 2015; Kuznetsova et al. 2022). This expectation appears to be borne out in the AB Aur system, which displays a ring and azimuthal asymmetry in mm continuum emission at $r \sim 1''$ (e.g., Figure 6, Tang et al. 2017), just interior to the merging zone identified here.

The sheer size of the AB Aur disk ($r \sim 1600$ au in ^{12}CO ; §2.3) may also be ascribed to late infall, as extraordinarily large disks are statistically more likely to have experienced infall with high angular momentum (Kuffmeier et al. 2023). Misalignment between the an-

gular momentum vector of infalling material and that of the inheriting disk can induce warping (Sai et al. 2020; Kuffmeier et al. 2021; Dullemond et al. 2022; Kuffmeier et al. 2024), with a severity that depends on the mass ratio of the two. Some degree of warping appears to be present in the AB Aur disk, based on the non-axisymmetry of the background velocity field traced by ^{13}CO and C^{18}O (Speedie et al. 2024).

5.3. How do we interpret the SO emission morphology?

SO emission in the AB Aur system has been observed in five transitions with three facilities to date: $\text{SO } 3_4 - 2_3$ and $5_6 - 4_5$ with the IRAM 30m telescope (Fuente et al. 2010, not spatially resolved); $\text{SO } 5_6 - 4_5$ with NOEMA in CD configuration (Pacheco-Vázquez et al. 2016, spatially resolved for the first time); $\text{SO } 5_5 - 4_4$ and $5_6 - 4_5$ with NOEMA in AC configuration (Rivière-Marichalar et al. 2020); and $\text{SO } 5_6 - 4_5$, $6_5 - 5_4$ and $6_7 - 5_6$ with ALMA (Dutrey et al. 2024). In the latter three works, where $\text{SO } 5_6 - 4_5$ is spatially resolved, a brightness peak within a ring of emission is found in the same location reported here. In this section, we discuss its production and survival.

The merging of S1 and S2 will be accompanied by shock waves if the infalling flow is supersonic. This is typically the case in infall, with the speed of sound being $\lesssim 0.2$ km/s at $r \gtrsim 100$ au. While we only measure line-of-sight velocities of S1 and S2 in the data (Figure 4), we can estimate their incident velocity using the known velocity components of the model streamlines, which are listed in Appendix Table 3. Their three velocity components (inward, clockwise, and toward the midplane) range 0.7–4.1 km/s, consistent with ‘low-velocity’ (usually quoted to mean 2 km/s) shocks.

Within shocks, the kinetic energy of the infalling material is converted into thermal energy. Dust grains are heated by conduction from the shocked gas, and by increased aerodynamic drag if the gas is decelerated by pressure forces (e.g., Miura et al. 2017). If the resulting dust temperature is sufficiently high (of order 40–70 K), SO can be produced directly via thermal sublimation of SO ice mantles (e.g., van Gelder et al. 2021). Within the SO ring in the AB Aur system, Rivière-Marichalar et al. (2020) and Pacheco-Vázquez et al. (2016) estimate an average gas kinematic temperature of ~ 39 K from H_2CO and SO multi-transition analysis. If aerodynamic heating operates alongside conductive heating, the gas kinematic temperature may represent a lower bound for the dust temperature.

Thermal sublimation is most efficient for small grains ($< 0.1 \mu\text{m}$) because they are more significantly heated, due to their lower emissivities (Miura et al. 2017). They also likely represent the largest contribution to the dust-grain surface area (e.g. Mathis et al. 1977). HST/STIS imaging of AB Aur at $0.57 \mu\text{m}$ wavelengths (tracing grain sizes $\lambda/2\pi \sim 0.09 \mu\text{m}$, e.g., Kruegel 2003) confirms such small grains are present high in the disk atmo-

sphere, and with a surface brightness distribution following S1 and S2 (Figure 5c; Grady et al. 1999).

Gas-phase formation of SO after the sputtering of s- CH_4 and s- H_2S may be an alternative possibility, in which case we should observe H_2CO and SH emission coincident with SO (van Gelder et al. 2021). Indeed, the former has been seen by Pacheco-Vázquez et al. (2016) and Rivière-Marichalar et al. (2020). On the other hand, sputtering has been found to only become relevant at larger shock velocities (> 10 km/s; Aota et al. 2015).

Regardless of which production mechanism, if SO is produced at the merging zone of S1 and S2, it would need to survive (only) ~ 3500 years to be circularized, based on the orbital period timescale, $P = r^{3/2} M_\star^{-1/2}$, at the outermost radius of the SO ring ($r \sim 300$ au). Chemical modeling of the AB Aur system by Pacheco-Vázquez et al. (2016) suggests SO molecules are depleted in less than 0.1 Myr (at densities $> 10^7 \text{ cm}^{-3}$ and assuming a fixed dust temperature of 45 K), which is a $\sim 30\times$ longer timescale. Looking toward other systems, there are cases where SO emission associated with the merging zone of infall has been observed as only a clump, rather than a ring, despite shorter circularization timescales: for example, DR Tau (Huang et al. 2024, 350 years), DG Tau and HL Tau (Garufi et al. 2022, 600–1200 years). We may conclude there are different physical conditions in these systems, or deeper observations may help to further illuminate the SO emission morphologies.

6. CONCLUSIONS

We have presented deep and high spectral resolution ALMA observations (ID: 2021.1.00690.S) of $^{12}\text{CO } J = 2 - 1$ and $\text{SO } J_N = 5_6 - 4_5$ emission toward the Class II YSO AB Aur. In ^{12}CO , we mapped three infalling ‘streamers’ spatially coincident with the disk, constrained their physical 3D geometries, and showed they can be modeled down to where they merge with the disk. A summary of our approach and findings is as follows.

- Using a combination of Keplerian and anti-Keplerian masking, we isolate the disk-like ^{12}CO emission from non-disk-like emission, which we term the ‘exo-disk’ component (§3.2).
- The disk emission of ^{12}CO extends up to ~ 1600 au in radius, and exhibits global spiral structure consistent with gravitational instability (Figure 3).
- Within the exo-disk emission, we re-detect the three ^{12}CO spiral structures S1, S2 and S3, first observed by Tang et al. (2012) with the PdBI. Using the ballistic accretion flow model of Mendoza et al. (2009) and Pineda et al. (2020), we reproduce the on-sky and position-velocity trajectories of S1, S2 and S3 in detail (Figure 4).

- Our modeling results indicate that S1 and S2 are infalling onto the disk from in front (Appendix Figure 10), consistent with their traces in HST/STIS imaging of $0.57\ \mu\text{m}$ scattered light (Figure 5).
- We identify the ‘merging zone’ of S1 and S2 as the region where their emission becomes indistinguishable with that of the disk in PV space (Figure 4 & 9), and where their model streamlines intersect with the disk midplane (Figure 10).
- The merging zone of S1 and S2 lies $15^\circ - 100^\circ$ east of north and $150 - 300$ au in radius on the sky, coincident with where a ring of SO emission exhibits a brightness asymmetry peaking at $2.5\times$ its azimuthal average level (Figure 5).

We consider infall to be a strong explanation for the observed gravitational instability and implied high disk mass in the AB Aur system (§5.2; Speedie et al. 2024). The origin of the infalling material in this system remains an open question (§5.1), though kinematic observations probing larger spatial scales may affirm the cloudlet capture hypothesis (Appendix Figure 8; Dullemond et al. 2019). Detailed kinematic investigations of how late-stage infall interfaces with the disk should be undertaken in a larger number of planet-forming systems to understand its influence on disk structure and the local planet formation environment.

7. ACKNOWLEDGMENTS

We thank our referee for providing a helpful review of the manuscript, including thoughtful suggestions and questions. We are grateful to Michael Kuffmeier, Álvaro Ribas, Adele Plunkett, Andrew Winter, Myriam Benisty, Pablo Rivière-Marichalar, Asunción Fuente, Takayuki Muto, Yifan Zhou and Sahl Rowther for enlightening discussions, and to Giulia Perotti for valuable comments on the manuscript. J.S. thanks Ryan Loomis, Sarah Wood and Tristan Ashton at the North American ALMA Science Center (NAASC) for providing science support and technical guidance on the ALMA data as part of a Data Reduction Visit to the NAASC, which was funded by the NAASC. The reduction and imaging of the ALMA data was performed on NAASC computing facilities.

J.S. acknowledges financial support from the Natural Sciences and Engineering Research Council of Canada (NSERC) through the Canada Graduate Scholarships Doctoral (CGS D) program. R.D. acknowledges financial support provided by the Natural Sciences and Engineering Research Council of Canada through a Discovery Grant, as well as the Alfred P. Sloan Foundation through a Sloan Research Fellowship. C.L. and G.L. acknowledge funding from the European Union’s Horizon 2020 research and innovation programme under the Marie Skłodowska-Curie grant agreement #

823823 (RISE DUSTBUSTERS project). C.L. acknowledges funding from UK Science and Technology research Council (STFC) via the consolidated grant ST/W000997/1. B.V. acknowledges funding from the ERC CoG project PODCAST No 864965. Y.W.T. acknowledges support through NSTC grant 111-2112-M-001-064- and 112-2112-M-001-066-. J.H. was supported by JSPS KAKENHI Grant Numbers 21H00059, 22H01274, 23K03463. J.C. acknowledges support from the National Natural Science Foundation of China under grant No. 12233004 and 12250610189. D.S.-C. is supported by an NSF Astronomy and Astrophysics Postdoctoral Fellowship under award AST-2102405.

This paper makes use of the following ALMA data: ADS/JAO.ALMA#2021.1.00690.S. ALMA is a partnership of ESO (representing its member states), NSF (USA) and NINS (Japan), together with NRC (Canada), MOST and ASIAA (Taiwan), and KASI (Republic of Korea), in cooperation with the Republic of Chile. The Joint ALMA Observatory is operated by ESO, AUI/NRAO and NAOJ. The National Radio Astronomy Observatory is a facility of the National Science Foundation operated under cooperative agreement by Associated Universities, Inc.

Based on data products created from observations collected at the European Organisation for Astronomical Research in the Southern Hemisphere under ESO programme 0104.C-0157(B). This work has made use of the SPHERE Data Centre, jointly operated by OSUG/IPAG (Grenoble), PYTHEAS/LAM/CESAM (Marseille), OCA/Lagrange (Nice), Observatoire de Paris/LESIA (Paris), and Observatoire de Lyon.

This research used the Canadian Advanced Network For Astronomy Research (CANFAR) operated in partnership by the Canadian Astronomy Data Centre and The Digital Research Alliance of Canada with support from the National Research Council of Canada the Canadian Space Agency, CANARIE and the Canadian Foundation for Innovation.

Based on observations made with the NASA/ESA Hubble Space Telescope, obtained from the Data Archive at the Space Telescope Science Institute, which is operated by the Association of Universities for Research in Astronomy, Inc., under NASA contract NAS5-26555. These observations are associated with program #8065.

Herschel is an ESA space observatory with science instruments provided by European-led Principal Investigator consortia and with important participation from NASA. PACS has been developed by a consortium of institutes led by MPE (Germany) and including UVIE (Austria); KU Leuven, CSL, IMEC (Belgium); CEA, LAM (France); MPIA (Germany); INAF-IFSI/OAA/OAP/OAT, LENS, SISSA (Italy); IAC (Spain). This development has been supported by the funding agencies BMVIT (Austria), ESA-PRODEX (Belgium), CEA/CNES (France), DLR (Germany),

ASI/INAF (Italy), and CICYT/MCYT (Spain). SPIRE has been developed by a consortium of institutes led by Cardiff University (UK) and including Univ. Lethbridge (Canada); NAOC (China); CEA, LAM (France); IFSI, Univ. Padua (Italy); IAC (Spain); Stockholm Observatory (Sweden); Imperial College London, RAL, UCL-MSSL, UKATC, Univ. Sussex (UK); and Caltech, JPL, NHSC, Univ. Colorado (USA). This development has been supported by national funding agencies: CSA (Canada); NAOC (China); CEA, CNES, CNRS (France); ASI (Italy); MCINN (Spain); SNSB (Sweden); STFC, UKSA (UK); and NASA (USA).

Facilities: ALMA, VLT, Herschel, HST

Software: `astropy` (Astropy Collaboration et al. 2013, 2018), `bettermoments` (Teague & Foreman-Mackey 2018a,b), `CASA` (McMullin et al. 2007), `CMasher` (van der Velden 2020), `gofish` (Teague 2019), `keplerian_mask` (Teague 2020), `matplotlib` (Hunter 2007), `numpy` (Harris et al. 2020), `pandas` (McKinney 2011), `pvextractor` (Robitaille et al. 2018), `pyvista` (Sullivan & Kaszynski 2019), `scipy` (Virtanen et al. 2020).

DATA AVAILABILITY

All ALMA data products presented in this work are available through the [CANFAR Data Publication Service](#) at [doi:10.11570/24.0098](https://doi.org/10.11570/24.0098). This includes final reduced and calibrated ALMA measurement sets, image cubes, masks and moment maps. The raw ALMA data are publicly available via the ALMA archive <https://almascience.nrao.edu/aq/> under project ID 2021.1.00690.S. Animations of Figures 2, 7, 8, 9, and 10 are available in the online Journal and on FigShare: [doi:10.6084/m9.figshare.28205066.v1](https://doi.org/10.6084/m9.figshare.28205066.v1).

APPENDIX

A. ROBUSTNESS OF SO BRIGHTNESS PEAK TO CONTINUUM SUBTRACTION

Figure 6 presents our ALMA continuum image at 1.3 mm alongside peak intensity and integrated intensity maps of SO $J_N = 5_6 - 4_5$ imaged with and without continuum subtraction. The SO ring peaks exterior to, but still overlaps with, the continuum ring (c.f. Fig. 2 of Dutrey et al. 2024). As seen in previous works (e.g., Tang et al. 2017; van der Marel et al. 2021; Rivière-Marichalar et al. 2024), the continuum ring exhibits an azimuthal asymmetry, concentrated on nearly the opposite side of the disk to the brightness peak in SO. We re-imaged the SO data without continuum subtraction to confirm the SO brightness peak is not the gas counterpart of the dust continuum asymmetry. As shown in the top row of Figure 6, the two *peak* intensity maps are very similar: the inclusion of the continuum extends the ring’s apparent width inward, but the exterior substructure is brighter than the continuum and remains unchanged. In contrast, the substructure seen in an *integrated* intensity map of SO is greatly influenced by the presence or subtraction of the continuum, as shown in the bottom row of Figure 6.

B. KEPLERIAN AND ANTI-KEPLERIAN MASKS

Our process to disentangle the bulk rotating component of ^{12}CO $J = 2 - 1$ emission from all other emission was inspired by Huang et al. (2021) and broadly follows their approach to isolate the extended ^{12}CO structures in GM Aur (see their Figure 17 and Appendix C).

First, we generate a Keplerian mask using the `keplerian_mask` script of Teague (2020). The result is a cube of the same dimensions as the data but filled with Boolean values reflecting the position-position-velocity (PPV) volume of the ^{12}CO emitting region (e.g., see §5.1 of Czekala et al. 2021). This volume is calculated given a specified stellar mass M_* , distance d , disk inclination i , position angle, systemic velocity v_{sys} , outer radius r_{out} , constant emission surface slope z/r , and intrinsic line width parameters ΔV_0 and ΔV_q . The intrinsic line width profile is described by:

$$\Delta V(r) = \Delta V_0 \left(\frac{r}{1''} \right)^{\Delta V_q}. \quad (\text{B1})$$

Table 2 lists the parameters we adopted. Our choices for r_{out} , z/r , ΔV_0 and ΔV_q were found by experimentation, with the goal of capturing the disk emission at large radii (made tricky by super-Keplerian rotation) while evading non-Keplerian emission at small radii (made tricky by S1). The `keplerian_mask` routine additionally offers the option to convolve the mask with a 2D Gaussian beam (of FWHM θ_{conv}) to account for emission broadening, which we opted not to do for simplicity.

Next, we generate an anti-Keplerian mask as an exact copy of the Keplerian mask but with its Boolean values switched (1s to 0s and vice versa). The result is a second cube of the same dimensions as the data, now with a ‘hole’ reflecting the PPV volume of the ^{12}CO emitting region.

The top half of Figure 7 provides a view of the Keplerian and anti-Keplerian masks at this stage in the process. For what follows, note that the spectrum in each spatial pixel of the Keplerian mask is a top hat function (and in the anti-Keplerian mask it is an upside-down top hat function).

From here, we perform post-processing on the masks to mitigate artifacts created in the moment maps from the hard (discontinuous) edges of the PPV volumes (c.f. Figure 17 of Huang et al. 2021). We spectrally smooth the masks by convolving the spectrum in each spatial pixel with a Gaussian 5 channels wide. This transforms Boolean masks into 3D weighting functions and has the desired effect of softening the edges of the PPV volumes. Insofar as the weights in the edges are modulated (from 1 to slightly less than 1, or from 0 to slightly more than 0), the spectral smoothing introduces ‘overlap’ between the PPV volumes in each cube. The bottom half of Figure 7 provides a view of the Keplerian and anti-Keplerian masks at the end of the process.

As a final note of nuance, we considered defining an anti-Keplerian mask as a Keplerian mask of opposite *inclination*; however, the resulting two masks would be identical at the disk minor axis, and ineffective at separating the ^{12}CO emission components identified here.

C. CONNECTION TO LARGER ENVIRONMENT

Figure 8 provides a multi-wavelength view of AB Aur’s environment from 10^5 au to 10^2 au scales. The top panel shows where AB Aur is situated within the L1517 cloud in the Taurus-Auriga complex (Luhman 2023; Garufi et al. 2024; Ribas et al. 2017), in photometric observations of dust emission from the Herschel SPIRE instrument (Pilbratt et al. 2010; Griffin et al. 2010) at $250 \mu\text{m}$. The second row of panels zooms into a $10' \times 10'$ square, and shows the location of AB Aur in Herschel PACS (Poglitsch et al. 2010) and SPIRE maps at increasing wavelengths ($70 \mu\text{m}$, $160 \mu\text{m}$, $250 \mu\text{m}$ and $350 \mu\text{m}$). These four maps are Level 2.5 data products retrieved from the Herschel Science Archive, from the Herschel Key Project Gould Belt Survey (André et al. 2010; HGBS Team 2020) with OBSIDs 1342204843 and 1342204844 (OD 492). SU Aurigae is within $3'$ of AB Aur on the sky. The bottom row zooms into a $38'' \times 38''$ square centered on AB Aur, showing the field of view of our ALMA observations outlined in yellow. In this panel we present a moment 0 map of ^{12}CO emission

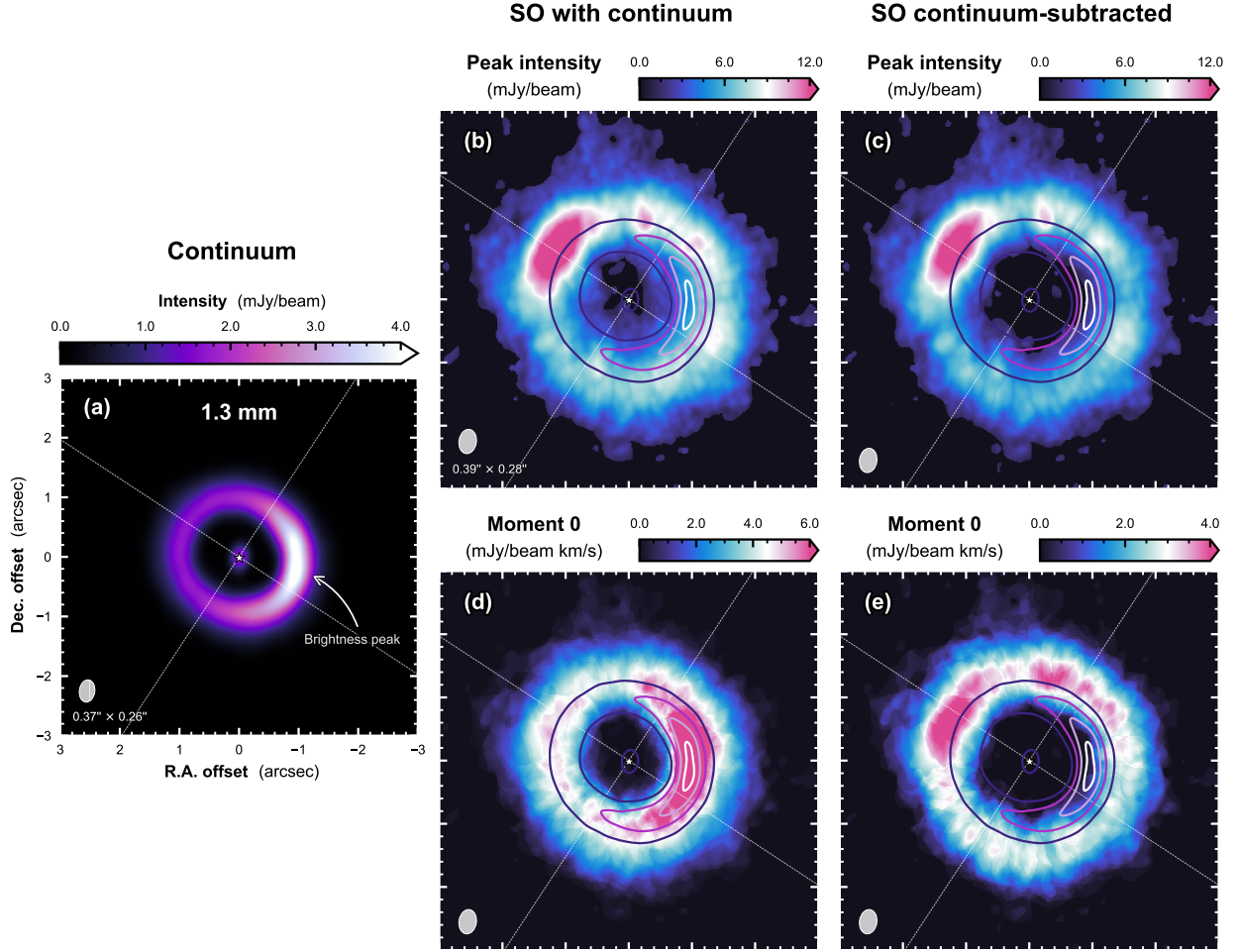


Figure 6. The influence of the continuum ring substructure on the observed SO ring substructure in peak intensity vs. integrated intensity maps. (a) ALMA continuum image at 233.0 GHz from the program presented in this work. The continuum is overlaid in contours at 1.0, 2.0, 3.0 and 4.0 mJy/beam in all other panels. (b) ALMA SO $J_N = 5_6 - 4_5$ peak intensity map before continuum subtraction, and (c) after continuum subtraction (shown in the main text). These two maps are shown on the same colorbar scale. (d) ALMA SO $J_N = 5_6 - 4_5$ integrated intensity map before and (e) after continuum subtraction.

Table 2. Keplerian Mask Parameters

Transition	M_\star ^a	d ^b	i ^c	P.A. ^a	v_{sys} ^a	r_{out}	ΔV_0	ΔV_q	z/r	θ_{conv}
	(M_\odot)	(pc)	($^\circ$)	($^\circ$)	(m/s)	($''$)	(m/s)			($''$)
$^{12}\text{CO } J = 2 - 1$	2.23	155.9	23.2	236.7	5850	20.0	700.0	0.0	0.0	None

^a Speedie et al. (2024). ^b Gaia Collaboration et al. (2023). ^c Tang et al. (2012, 2017).

imaged with a Briggs weighting of `robust=1.5`, showing the faint ‘tail-like’ emission structure extending from the disk to the south. We stress that this image has not been primary beam corrected (see below). In the bottom left panel, we overlay the ALMA field of view as a yellow circle onto the R -band (647 nm) image toward AB Aur obtained by the University of Hawaii 2.2 m Telescope (Grady et al. 1999; Nakajima & Golimowski 1995) showing the arc-shaped reflection nebula surrounding

AB Aur from the east to the south (Dullemond et al. 2019; Kuffmeier et al. 2020; Gupta et al. 2023).

While a detailed kinematic analysis is outside the scope of this work, we describe that the ^{12}CO tail is comprised of subcomponents: the first is observed blueshifted of v_{sys} (between 5.010–5.850 km/s in LSRK) due south of the star, and the second is observed redshifted of v_{sys} (between 5.976 – 6.942 km/s in LSRK) ever so slightly counter-clockwise of south. The latter

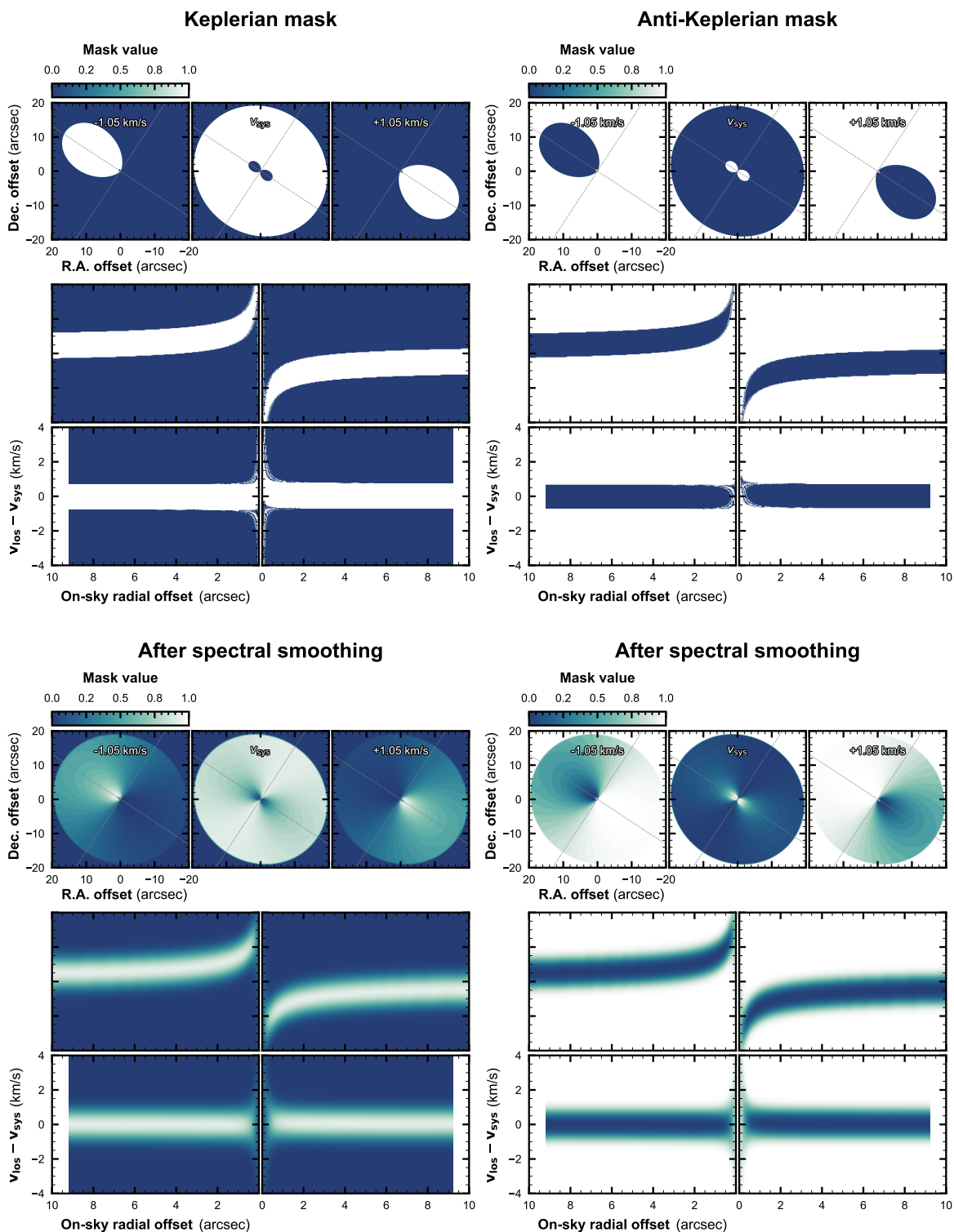


Figure 7. A presentation of the Keplerian and anti-Keplerian masks. **Top:** Boolean versions prior to spectral smoothing. The topmost panels show three channel maps from the masks at three demonstrative velocities. The panels immediately below show PV slices taken through the masks along the disk major and minor axes, as in Figure 2. **Bottom:** Smoothed versions after convolving the spectra in each spatial pixel of the masks with a Gaussian kernel. These are used as 3D weighting functions to separate the observed ^{12}CO emission into its constituent disk and exo-disk components. An animation of the Keplerian and anti-Keplerian masks is [available](#) in the online Journal. The animation shows the channel maps of the two masks before (top row) and after (bottom row) spectral smoothing, panning through the imaged spectral axis from -0.198 to 12.444 km/s in 0.042 km/s LSRK velocity channels.

exhibits a substructure like three ‘whiskers’ over several channels. Animated ^{12}CO channel maps are available (Figure 8) in the online article.

As discussed in §5.1, our detection of the ^{12}CO tail suffers from the reduced response of the ALMA 12m antenna at the edge of our imaged FOV, where the sensitivity is $5\times$ lower than at the pointing center, and, as stressed above, the image in Figure 8 has not been corrected for this effect. We show the non-primary beam corrected image without the quantification of a colorbar to reflect that it should be considered for morphology only. Aliases of the tail also appear multiple times around the edge of the FOV. Such aliasing artifacts are known to be introduced by bright sources outside the primary beam (ALMA Technical Handbook, §11.5). Observations with a larger FOV and sensitivity to larger spatial scales are needed to achieve improved sensitivity to extended emission, in order to investigate the ^{12}CO tail and hypothesized association between the clouddlet.

D. RADIAL AND AZIMUTHAL PV SLICES

Figure 9 explores the trajectories of S1, S2 and S3 in radial and azimuthal PV diagrams. The left column of Figure 9 shows radial PV cross sections at varying azimuths around the eastern (blueshifted) major axis. The right column shows azimuthal PV cross sections at varying radii between $r = 1'' - 2''$. As in the main text, the background colormap shows slices taken through the (unmasked) ^{12}CO image cube, and the filled contours are from slices taken through the SO image cube. Orange contours are overplotted using slices through the Keplerian weighted ^{12}CO cube to delineate emission associated with the disk. Cyan contours encircle S1, S2 and S3 from slices through the anti-Keplerian weighted ^{12}CO cube. We inspected a fine and complete grid of PV slice orientations to build an understanding of their v_{LOS} behaviour as a function of azimuth and radius, available as animations in the online article. A representative selection of slices is shown in Figure 9, demonstrating where ^{12}CO emission from S1 and S2 becomes indistinguishable from the emission from the disk.

E. STREAMLINE PARAMETERS AND 3D RENDERING

Table 3 provides the parameters describing the streamline solutions presented in §4.2. The angular frequency of the sphere’s rigid-body rotation is represented by Ω , and r_0 is its radius. The initial radial velocity of the ‘particle’ is $v_{r,0}$, while ϕ_0 and θ_0 are its initial azimuthal and polar angles, respectively. θ_0 is measured from the positive z axis (such that $\theta_0 = 90^\circ$ defines the sphere’s equatorial plane), and ϕ_0 is measured from the positive x axis toward the positive y axis. The angles i_{pims} and PA_{pims} are used in the two rotational transformations to project the streamline’s ‘native’ coordinates onto the sky. The inclination i_{pims} defines rotation about the native x axis, and negative inclination corre-

sponds to viewing the sphere’s midplane ‘‘from below’’, i.e., up from along the negative z axis. PA_{pims} is defined as rotation about the native y axis, where $\text{PA}_{\text{pims}} = 0^\circ$ aligns minor axis of the midplane with north.

Following the discussion in §5.3, we provide the intrinsic velocity components at the terminal ends of the three model streamlines in the frame of the rigid rotating sphere: the inward radial velocity $v_{r,\text{term}}$, the azimuthal velocity $v_{\phi,\text{term}}$, and the downward vertical velocity $v_{z,\text{term}}$ (Table 3). The terminal velocities of the S1 and S2 streamlines range $0.7 - 4.1$ km/s. Table 3 also lists the streamlines’ centrifugal radii, r_{cent} . Sakai et al. (2014) connected an observed enhancement of SO to the centrifugal radius in ALMA observations of L1527, which has since been seen in more sources (e.g., Oya et al. 2016; Sakai et al. 2017). Our model streamline solution for S1 has a centrifugal radius of ~ 350 au, conspicuously close to the observed radius of the SO ring ($150 - 300$ au). For S2 the value is larger (~ 550 au). We caution direct comparisons here though: since the model is ballistic, angular momentum loss by friction is not considered.

In Figure 10, we show a rendering of the disk+streamline system in 3D spatial coordinates, $\langle \text{RA}, \text{Dec}, \text{LOS} \rangle$, using the software `pyvista` (Sullivan & Kaszynski 2019). The SO peak intensity map is rendered, semi-transparent, onto a planar disk with the orientation of AB Aur’s midplane for comparison with the terminal ends of S1 and S2. It is significant that despite letting all parameters vary (save for the central mass M ; §4.1), we find a family of streamline solutions for each of S1 and S2 that are physically coherent in 3D spatial coordinates.

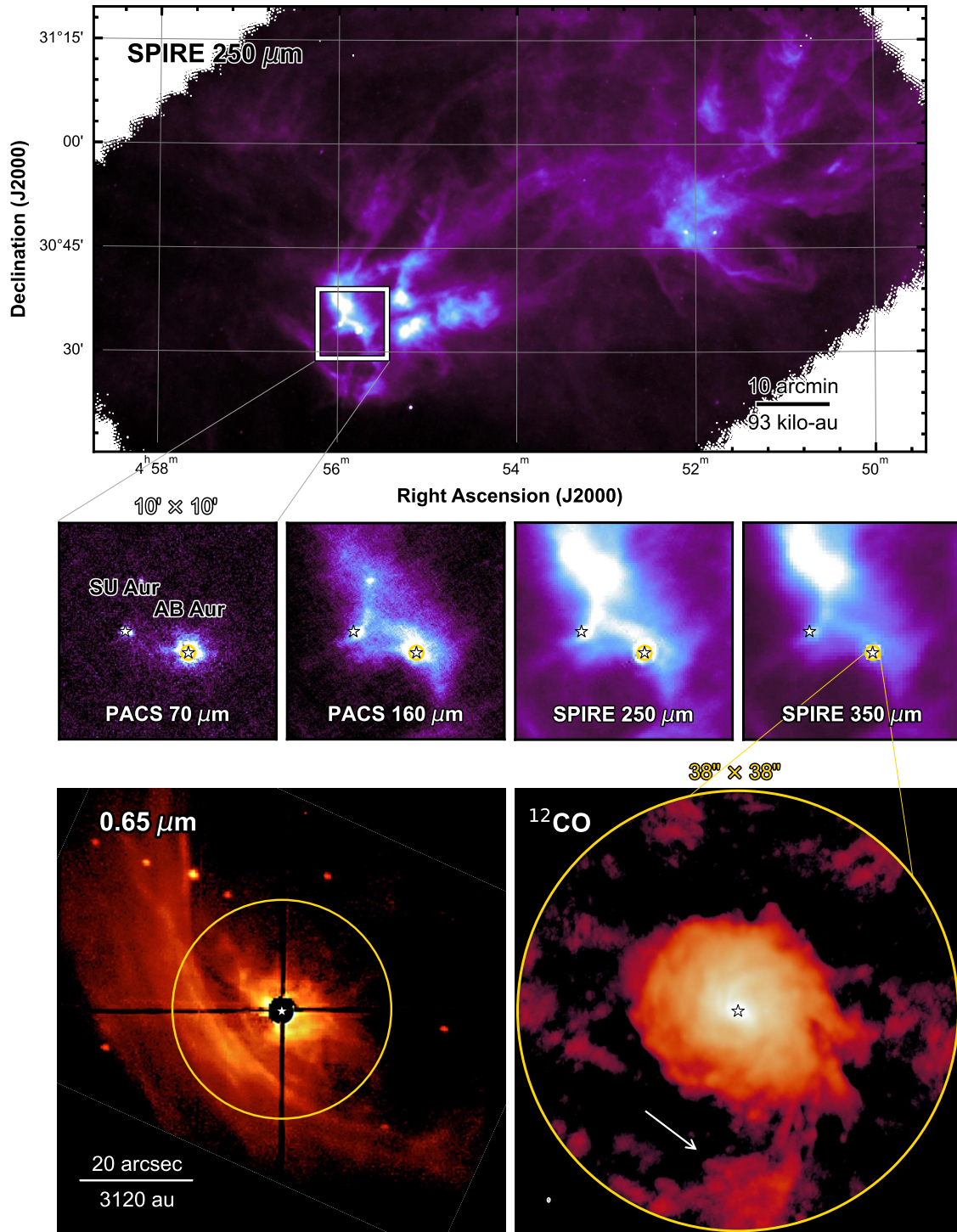


Figure 8. Multi-wavelength view of AB Aur’s kilo-au environment and a tentative tail in ^{12}CO . **Top:** Herschel SPIRE $250\ \mu\text{m}$ map of the L1517 cloud. A scale bar in the bottom right corner shows $10'$ or 93 kilo-au. **Middle:** $10' \times 10'$ zoom-in toward AB Aur in Herschel PACS and SPIRE maps at $70\ \mu\text{m}$, $160\ \mu\text{m}$, $250\ \mu\text{m}$ and $350\ \mu\text{m}$. The location of SU Aurigae is also marked. **Bottom right:** ALMA $^{12}\text{CO}\ J = 2 - 1$ moment 0 map, imaged with Briggs `robust=1.5` and without primary beam correction. The white arrow points to the tail. In the online Journal, an animation is [available](#) to show the tail in the ^{12}CO channel maps. In the animation, intensity (horizontal colorbar) spans only $\pm 5\sigma$, and the LSRK velocity of the channel (vertical colorbar) is represented by the background color outside the ALMA FOV. **Bottom left:** Optical image toward AB Aur at 647 nm from the University of Hawaii 2.2 m Telescope (PI: P. Kalas; Grady et al. 1999). This image is used with permission of P. Kalas. In all panels, the yellow circle marks the edge of our imaged ALMA field of view (§2).

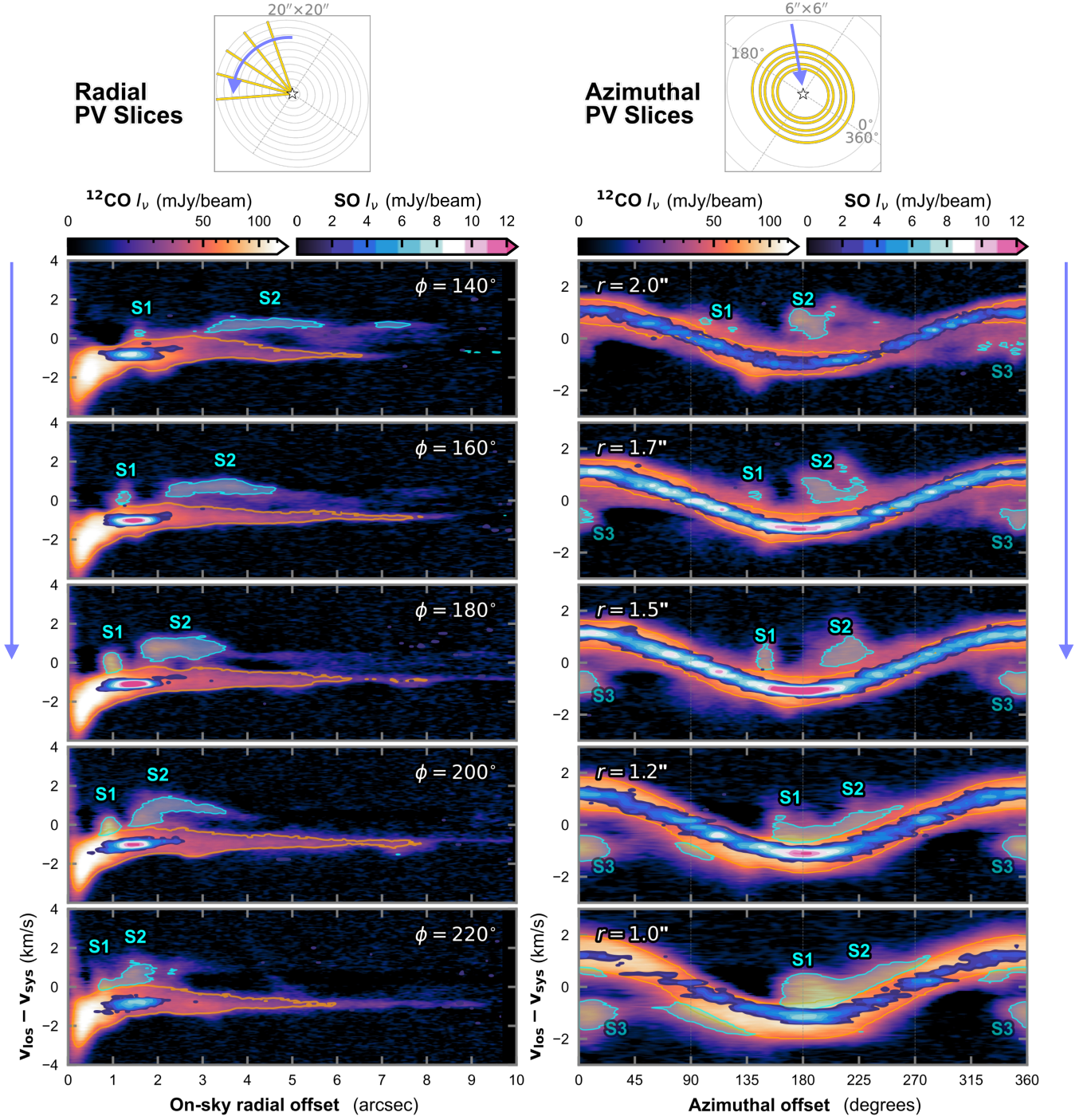


Figure 9. Radial and azimuthal PV cross sections in ^{12}CO and SO . The yellow lines and circles in the diagram above each column shows the slice paths of the PV diagrams in the panels below. In the left column, panels are ordered top to bottom by their azimuthal angle in the direction the disk rotates (counter-clockwise). In the right column, panels are ordered by decreasing radius. PV slices are shown for the three ^{12}CO cubes: the full unweighted ^{12}CO cube (colormap), the Keplerian weighted ^{12}CO cube (orange contours), and the anti-Keplerian weighted ^{12}CO cube (cyan contours). PV slices in the $\text{SO } J_N = 5_6 - 4_5$ image cube are overplotted as filled contours in increments of 2σ starting at 3σ . A set of animations for this figure is available in the online Journal. Three animations are concatenated and played sequentially. At $t = 3\text{s}$: The radial PV slices panning through all azimuthal angles (same as Figure 2). At $t = 29\text{s}$: The azimuthal PV slices, panning from $r = 12''$ to $0''$. At $t = 69\text{s}$: A repeat of the azimuthal PV slices, using a varying colorbar to reveal features at large radii.

Table 3. Parameters describing the PIMS streamline solutions, and resulting properties.

Streamline	Ω	r_0	$v_{r,0}$	ϕ_0	θ_0	i_{pims}	PA_{pims}	r_{cent}	$v_{r,\text{term}}$	$v_{\phi,\text{term}}$	$v_{z,\text{term}}$
	(Hz)	(au)	(km/s)	($^\circ$)	($^\circ$)	($^\circ$)	($^\circ$)	(au)	(km/s)	(km/s)	(km/s)
S1	1.50×10^{-11}	650	1.5	374	80	-56.8	43.3	350	1.4	4.1	0.7
S2	8.00×10^{-12}	1000	1.0	30	55	-56.8	53.3	557	1.7	3.0	2.0
S3	1.40×10^{-11}	325	0.25	290	135	-66.8	33.3	19	5.4	1.3	3.3

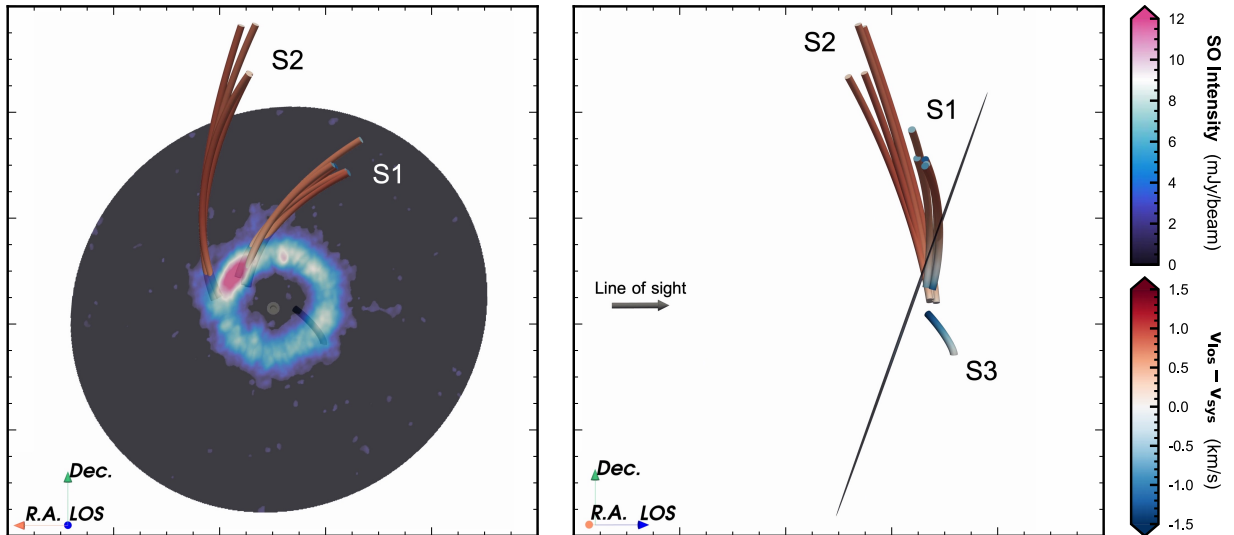


Figure 10. 3D rendering of the AB Aur disk plane and streamline solutions. The left panel shows the system oriented as viewed from Earth (the RA-Dec plane), and the right panel shows a view from within the plane of the sky (the Dec-LOS plane). The streamlines are rendered as ‘tubes’ and coloured by their line-of-sight velocity, v_{LOS} . The SO peak intensity map is rendered onto a disk with same orientation as the AB Aur midplane. The layer is given 80% transparency to show objects behind the disk. An animation of this figure is [available](#) in the online Journal, in which the viewing angle is rotated 360° about the declination axis to clearly illustrate the 3D geometry. This rendering was enabled by `pyvista` (Sullivan & Kaszynski 2019).

REFERENCES

- André, P., Men'shchikov, A., Bontemps, S., et al. 2010, *A&A*, 518, L102, doi: [10.1051/0004-6361/201014666](https://doi.org/10.1051/0004-6361/201014666)
- Andrews, S. M., Teague, R., Wirth, C. P., Huang, J., & Zhu, Z. 2024, *ApJ*, 970, 153, doi: [10.3847/1538-4357/ad5285](https://doi.org/10.3847/1538-4357/ad5285)
- Aota, T., Inoue, T., & Aikawa, Y. 2015, *ApJ*, 799, 141, doi: [10.1088/0004-637X/799/2/141](https://doi.org/10.1088/0004-637X/799/2/141)
- Astropy Collaboration, Robitaille, T. P., Tollerud, E. J., et al. 2013, *A&A*, 558, A33, doi: [10.1051/0004-6361/201322068](https://doi.org/10.1051/0004-6361/201322068)
- Astropy Collaboration, Price-Whelan, A. M., Sipőcz, B. M., et al. 2018, *AJ*, 156, 123, doi: [10.3847/1538-3881/aabc4f](https://doi.org/10.3847/1538-3881/aabc4f)
- Bae, J., Hartmann, L., & Zhu, Z. 2015, *ApJ*, 805, 15, doi: [10.1088/0004-637X/805/1/15](https://doi.org/10.1088/0004-637X/805/1/15)
- Beck, T. L., & Bary, J. S. 2019, *ApJ*, 884, 159, doi: [10.3847/1538-4357/ab4259](https://doi.org/10.3847/1538-4357/ab4259)
- Berghea, C. T., Bayyari, A., Sitko, M. L., et al. 2024, *ApJL*, 967, L3, doi: [10.3847/2041-8213/ad43e3](https://doi.org/10.3847/2041-8213/ad43e3)
- Biddle, L. I., Bowler, B. P., Zhou, Y., Franson, K., & Zhang, Z. 2024, *AJ*, 167, 172, doi: [10.3847/1538-3881/ad2a52](https://doi.org/10.3847/1538-3881/ad2a52)
- Boccaletti, A., Di Folco, E., Pantin, E., et al. 2020, *A&A*, 637, L5, doi: [10.1051/0004-6361/202038008](https://doi.org/10.1051/0004-6361/202038008)
- Bondi, H. 1952, *MNRAS*, 112, 195, doi: [10.1093/mnras/112.2.195](https://doi.org/10.1093/mnras/112.2.195)
- Bouwman, J., de Koter, A., van den Ancker, M. E., & Waters, L. B. F. M. 2000, *A&A*, 360, 213
- Braun, R., & Waltherbos, R. A. M. 1985, *A&A*, 143, 307
- Cacciapuoti, L., Macias, E., Gupta, A., et al. 2024, *A&A*, 682, A61, doi: [10.1051/0004-6361/202347486](https://doi.org/10.1051/0004-6361/202347486)
- Calcino, J., Price, D. J., Hilder, T., et al. 2024, arXiv e-prints, arXiv:2410.18521, doi: [10.48550/arXiv.2410.18521](https://doi.org/10.48550/arXiv.2410.18521)
- Cornwell, T. J. 2008, *IEEE Journal of Selected Topics in Signal Processing*, 2, 793, doi: [10.1109/JSTSP.2008.2006388](https://doi.org/10.1109/JSTSP.2008.2006388)
- Currie, T. 2024, *Research Notes of the American Astronomical Society*, 8, 146, doi: [10.3847/2515-5172/ad50ce](https://doi.org/10.3847/2515-5172/ad50ce)
- Currie, T., Lawson, K., Schneider, G., et al. 2022, *Nature Astronomy*, 6, 751, doi: [10.1038/s41550-022-01634-x](https://doi.org/10.1038/s41550-022-01634-x)
- Czekala, I., Loomis, R. A., Teague, R., et al. 2021, *ApJS*, 257, 2, doi: [10.3847/1538-4365/ac1430](https://doi.org/10.3847/1538-4365/ac1430)
- DeWarf, L. E., Sepinsky, J. F., Guinan, E. F., Ribas, I., & Nadalin, I. 2003, *ApJ*, 590, 357, doi: [10.1086/374979](https://doi.org/10.1086/374979)
- Dipierro, G., Lodato, G., Testi, L., & de Gregorio Monsalvo, I. 2014, *MNRAS*, 444, 1919, doi: [10.1093/mnras/stu1584](https://doi.org/10.1093/mnras/stu1584)
- Dong, R., Fung, J., & Chiang, E. 2016, *ApJ*, 826, 75, doi: [10.3847/0004-637X/826/1/75](https://doi.org/10.3847/0004-637X/826/1/75)
- Dullemond, C. P., Kimmig, C. N., & Zanazzi, J. J. 2022, *MNRAS*, 511, 2925, doi: [10.1093/mnras/stab2791](https://doi.org/10.1093/mnras/stab2791)
- Dullemond, C. P., Küffmeier, M., Goicovic, F., et al. 2019, *A&A*, 628, A20, doi: [10.1051/0004-6361/201832632](https://doi.org/10.1051/0004-6361/201832632)
- Dutrey, A., Chapillon, E., Guilloteau, S., et al. 2024, arXiv e-prints, arXiv:2408.14276, doi: [10.48550/arXiv.2408.14276](https://doi.org/10.48550/arXiv.2408.14276)
- Edgar, R. 2004, *NewAR*, 48, 843, doi: [10.1016/j.newar.2004.06.001](https://doi.org/10.1016/j.newar.2004.06.001)
- Ediss, G. A., Carter, M., Cheng, J., et al. 2004, in *Fifteenth International Symposium on Space Terahertz Technology*, ed. G. Narayanan, 181–188
- Faridani, S., Bigiel, F., Flöer, L., Kerp, J., & Stanimirović, S. 2018, *Astronomische Nachrichten*, 339, 87, doi: [10.1002/asna.201713381](https://doi.org/10.1002/asna.201713381)
- Flores, C., Ohashi, N., Tobin, J. J., et al. 2023, *ApJ*, 958, 98, doi: [10.3847/1538-4357/acf7c1](https://doi.org/10.3847/1538-4357/acf7c1)
- Fuente, A., Cernicharo, J., Agúndez, M., et al. 2010, *A&A*, 524, A19, doi: [10.1051/0004-6361/201014905](https://doi.org/10.1051/0004-6361/201014905)
- Fukagawa, M., Hayashi, M., Tamura, M., et al. 2004, *ApJL*, 605, L53, doi: [10.1086/420699](https://doi.org/10.1086/420699)
- Gaia Collaboration, Vallenari, A., Brown, A. G. A., et al. 2023, *A&A*, 674, A1, doi: [10.1051/0004-6361/202243940](https://doi.org/10.1051/0004-6361/202243940)
- Garufi, A., Podio, L., Codella, C., et al. 2022, *A&A*, 658, A104, doi: [10.1051/0004-6361/202141264](https://doi.org/10.1051/0004-6361/202141264)
- Garufi, A., Ginski, C., van Holstein, R. G., et al. 2024, *A&A*, 685, A53, doi: [10.1051/0004-6361/202347586](https://doi.org/10.1051/0004-6361/202347586)
- Ginski, C., Facchini, S., Huang, J., et al. 2021, *ApJL*, 908, L25, doi: [10.3847/2041-8213/abdf57](https://doi.org/10.3847/2041-8213/abdf57)
- Grady, C. A., Woodgate, B., Bruhweiler, F. C., et al. 1999, *ApJL*, 523, L151, doi: [10.1086/312270](https://doi.org/10.1086/312270)
- Griffin, M. J., Abergel, A., Abreu, A., et al. 2010, *A&A*, 518, L3, doi: [10.1051/0004-6361/201014519](https://doi.org/10.1051/0004-6361/201014519)
- Gupta, A., Miotello, A., Williams, J. P., et al. 2024, *A&A*, 683, A133, doi: [10.1051/0004-6361/202348007](https://doi.org/10.1051/0004-6361/202348007)
- Gupta, A., Miotello, A., Manara, C. F., et al. 2023, *A&A*, 670, L8, doi: [10.1051/0004-6361/202245254](https://doi.org/10.1051/0004-6361/202245254)
- Hall, C., Dong, R., Rice, K., et al. 2019, *ApJ*, 871, 228, doi: [10.3847/1538-4357/aafac2](https://doi.org/10.3847/1538-4357/aafac2)
- Hall, C., Dong, R., Teague, R., et al. 2020, *ApJ*, 904, 148, doi: [10.3847/1538-4357/abac17](https://doi.org/10.3847/1538-4357/abac17)
- Hanawa, T., Garufi, A., Podio, L., Codella, C., & Segura-Cox, D. 2024, *MNRAS*, 528, 6581, doi: [10.1093/mnras/stae338](https://doi.org/10.1093/mnras/stae338)
- Harada, N., Tokuda, K., Yamasaki, H., et al. 2023, *ApJ*, 945, 63, doi: [10.3847/1538-4357/acb930](https://doi.org/10.3847/1538-4357/acb930)
- Harris, C. R., Millman, K. J., van der Walt, S. J., et al. 2020, *Nature*, 585, 357, doi: [10.1038/s41586-020-2649-2](https://doi.org/10.1038/s41586-020-2649-2)

- Harsono, D., Alexander, R. D., & Levin, Y. 2011, *MNRAS*, 413, 423, doi: [10.1111/j.1365-2966.2010.18146.x](https://doi.org/10.1111/j.1365-2966.2010.18146.x)
- Hennebelle, P., Lesur, G., & Fromang, S. 2017, *A&A*, 599, A86, doi: [10.1051/0004-6361/201629779](https://doi.org/10.1051/0004-6361/201629779)
- Henning, T., Burkert, A., Launhardt, R., Leinert, C., & Stecklum, B. 1998, *A&A*, 336, 565
- HGBS Team. 2020, Herschel Gould Belt Survey, IPAC, doi: [10.26131/IRSA72](https://doi.org/10.26131/IRSA72)
- Holdaway, M. A. 1999, in *Astronomical Society of the Pacific Conference Series*, Vol. 180, *Synthesis Imaging in Radio Astronomy II*, ed. G. B. Taylor, C. L. Carilli, & R. A. Perley, 401
- Huang, J., Bergin, E. A., Le Gal, R., et al. 2024, arXiv e-prints, arXiv:2407.01679, doi: [10.48550/arXiv.2407.01679](https://doi.org/10.48550/arXiv.2407.01679)
- Huang, J., Bergin, E. A., Öberg, K. I., et al. 2021, *ApJS*, 257, 19, doi: [10.3847/1538-4365/ac143e](https://doi.org/10.3847/1538-4365/ac143e)
- Hunter, J. D. 2007, *Computing in Science & Engineering*, 9, 90, doi: [10.1109/MCSE.2007.55](https://doi.org/10.1109/MCSE.2007.55)
- Jorsater, S., & van Moorsel, G. A. 1995, *AJ*, 110, 2037, doi: [10.1086/117668](https://doi.org/10.1086/117668)
- Kratter, K., & Lodato, G. 2016, *ARA&A*, 54, 271, doi: [10.1146/annurev-astro-081915-023307](https://doi.org/10.1146/annurev-astro-081915-023307)
- Kruegel, E. 2003, *The physics of interstellar dust*, IoP Series in astronomy and astrophysics (Bristol, UK: The Institute of Physics)
- Kuffmeier, M., Dullemond, C. P., Reissl, S., & Goicovic, F. G. 2021, *A&A*, 656, A161, doi: [10.1051/0004-6361/202039614](https://doi.org/10.1051/0004-6361/202039614)
- Kuffmeier, M., Frimann, S., Jensen, S. S., & Haugbølle, T. 2018, *MNRAS*, 475, 2642, doi: [10.1093/mnras/sty024](https://doi.org/10.1093/mnras/sty024)
- Kuffmeier, M., Goicovic, F. G., & Dullemond, C. P. 2020, *A&A*, 633, A3, doi: [10.1051/0004-6361/201936820](https://doi.org/10.1051/0004-6361/201936820)
- Kuffmeier, M., Jensen, S. S., & Haugbølle, T. 2023, *European Physical Journal Plus*, 138, 272, doi: [10.1140/epjp/s13360-023-03880-y](https://doi.org/10.1140/epjp/s13360-023-03880-y)
- Kuffmeier, M., Pineda, J. E., Segura-Cox, D., & Haugbølle, T. 2024, arXiv e-prints, arXiv:2405.12670, doi: [10.48550/arXiv.2405.12670](https://doi.org/10.48550/arXiv.2405.12670)
- Kuznetsova, A., Bae, J., Hartmann, L., & Mac Low, M.-M. 2022, *ApJ*, 928, 92, doi: [10.3847/1538-4357/ac54a8](https://doi.org/10.3847/1538-4357/ac54a8)
- Leroy, A. K., Hughes, A., Liu, D., et al. 2021, *ApJS*, 255, 19, doi: [10.3847/1538-4365/abec80](https://doi.org/10.3847/1538-4365/abec80)
- Lesur, G., Hennebelle, P., & Fromang, S. 2015, *A&A*, 582, L9, doi: [10.1051/0004-6361/201526734](https://doi.org/10.1051/0004-6361/201526734)
- Lodato, G., Rampinelli, L., Viscardi, E., et al. 2023, *MNRAS*, 518, 4481, doi: [10.1093/mnras/stac3223](https://doi.org/10.1093/mnras/stac3223)
- Longarini, C., Lodato, G., Toci, C., et al. 2021, *ApJL*, 920, L41, doi: [10.3847/2041-8213/ac2df6](https://doi.org/10.3847/2041-8213/ac2df6)
- Luhman, K. L. 2023, *AJ*, 165, 37, doi: [10.3847/1538-3881/ac9da3](https://doi.org/10.3847/1538-3881/ac9da3)
- Martire, P., Longarini, C., Lodato, G., et al. 2024, *A&A*, 686, A9, doi: [10.1051/0004-6361/202348546](https://doi.org/10.1051/0004-6361/202348546)
- Mathis, J. S., Rumpl, W., & Nordsieck, K. H. 1977, *ApJ*, 217, 425, doi: [10.1086/155591](https://doi.org/10.1086/155591)
- McKinney, W. 2011, *Python for High Performance and Scientific Computing*, 14, 1
- McMullin, J. P., Waters, B., Schiebel, D., Young, W., & Golap, K. 2007, in *Astronomical Society of the Pacific Conference Series*, Vol. 376, *Astronomical Data Analysis Software and Systems XVI*, ed. R. A. Shaw, F. Hill, & D. J. Bell, 127
- Mendoza, S., Tejada, E., & Nagel, E. 2009, *MNRAS*, 393, 579, doi: [10.1111/j.1365-2966.2008.14210.x](https://doi.org/10.1111/j.1365-2966.2008.14210.x)
- Miura, H., Yamamoto, T., Nomura, H., et al. 2017, *ApJ*, 839, 47, doi: [10.3847/1538-4357/aa67df](https://doi.org/10.3847/1538-4357/aa67df)
- Monsch, K., Lovell, J. B., Berghea, C. T., et al. 2024, *ApJL*, 967, L2, doi: [10.3847/2041-8213/ad3bb0](https://doi.org/10.3847/2041-8213/ad3bb0)
- Mori, S., Aikawa, Y., Oya, Y., Yamamoto, S., & Sakai, N. 2024, *ApJ*, 961, 31, doi: [10.3847/1538-4357/ad0634](https://doi.org/10.3847/1538-4357/ad0634)
- Nakajima, T., & Golimowski, D. A. 1995, *AJ*, 109, 1181, doi: [10.1086/117351](https://doi.org/10.1086/117351)
- Newton, I. 1687, *Philosophiae Naturalis Principia Mathematica.*, doi: [10.3931/e-rara-440](https://doi.org/10.3931/e-rara-440)
- Oya, Y., Sakai, N., López-Sepulcre, A., et al. 2016, *ApJ*, 824, 88, doi: [10.3847/0004-637X/824/2/88](https://doi.org/10.3847/0004-637X/824/2/88)
- Pacheco-Vázquez, S., Fuente, A., Baruteau, C., et al. 2016, *A&A*, 589, A60, doi: [10.1051/0004-6361/201527089](https://doi.org/10.1051/0004-6361/201527089)
- Paneque-Carreño, T., Pérez, L. M., Benisty, M., et al. 2021, *ApJ*, 914, 88, doi: [10.3847/1538-4357/abf243](https://doi.org/10.3847/1538-4357/abf243)
- Pelkonen, V.-M., Padoan, P., Juvela, M., Haugbølle, T., & Nordlund, Å. 2024, arXiv e-prints, arXiv:2405.06520, doi: [10.48550/arXiv.2405.06520](https://doi.org/10.48550/arXiv.2405.06520)
- Pilbratt, G. L., Riedinger, J. R., Passvogel, T., et al. 2010, *A&A*, 518, L1, doi: [10.1051/0004-6361/201014759](https://doi.org/10.1051/0004-6361/201014759)
- Pineda, J. E., Segura-Cox, D., Caselli, P., et al. 2020, *Nature Astronomy*, 4, 1158, doi: [10.1038/s41550-020-1150-z](https://doi.org/10.1038/s41550-020-1150-z)
- Pineda, J. E., Arzoumanian, D., Andre, P., et al. 2023, in *Astronomical Society of the Pacific Conference Series*, Vol. 534, *Protostars and Planets VII*, ed. S. Inutsuka, Y. Aikawa, T. Muto, K. Tomida, & M. Tamura, 233, doi: [10.48550/arXiv.2205.03935](https://doi.org/10.48550/arXiv.2205.03935)
- Poglitsch, A., Waelkens, C., Geis, N., et al. 2010, *A&A*, 518, L2, doi: [10.1051/0004-6361/201014535](https://doi.org/10.1051/0004-6361/201014535)
- Remijan, A., Biggs, A., Cortes, P. A., et al. 2019, *ALMA Technical Handbook, ALMA Doc. 7.3, ver. 1.1, 2019, ALMA Technical Handbook, ALMA Doc. 7.3, ver. 1.1* ISBN 978-3-923524-66-2, doi: [10.5281/zenodo.4511522](https://doi.org/10.5281/zenodo.4511522)

- Ribas, Á., Espaillat, C. C., Macías, E., et al. 2017, *ApJ*, 849, 63, doi: [10.3847/1538-4357/aa8e99](https://doi.org/10.3847/1538-4357/aa8e99)
- Rivière-Marichalar, P., Fuente, A., Le Gal, R., et al. 2020, *A&A*, 642, A32, doi: [10.1051/0004-6361/202038549](https://doi.org/10.1051/0004-6361/202038549)
- Rivière-Marichalar, P., Macías, E., Baruteau, C., et al. 2024, *A&A*, 683, A141, doi: [10.1051/0004-6361/202347464](https://doi.org/10.1051/0004-6361/202347464)
- Robitaille, T., Beaumont, C., Qian, P., Borkin, M., & Goodman, A. 2018, glueviz v0.13.1: multidimensional data exploration, 0.13.1, Zenodo, doi: [10.5281/zenodo.1237692](https://doi.org/10.5281/zenodo.1237692)
- Rowther, S., Price, D. J., Pinte, C., et al. 2024, *MNRAS*, doi: [10.1093/mnras/stae2167](https://doi.org/10.1093/mnras/stae2167)
- Sai, J., Ohashi, N., Saigo, K., et al. 2020, *ApJ*, 893, 51, doi: [10.3847/1538-4357/ab8065](https://doi.org/10.3847/1538-4357/ab8065)
- Sakai, N., Sakai, T., Hirota, T., et al. 2014, *Nature*, 507, 78, doi: [10.1038/nature13000](https://doi.org/10.1038/nature13000)
- Sakai, N., Oya, Y., Higuchi, A. E., et al. 2017, *MNRAS*, 467, L76, doi: [10.1093/mnrasl/slx002](https://doi.org/10.1093/mnrasl/slx002)
- Speedie, J., Dong, R., Hall, C., et al. 2024, arXiv e-prints, arXiv:2409.02196, doi: [10.48550/arXiv.2409.02196](https://doi.org/10.48550/arXiv.2409.02196)
- Sullivan, C. B., & Kaszynski, A. 2019, *Journal of Open Source Software*, 4, 1450, doi: [10.21105/joss.01450](https://doi.org/10.21105/joss.01450)
- Tang, Y. W., Guilloteau, S., Piétu, V., et al. 2012, *A&A*, 547, A84, doi: [10.1051/0004-6361/201219414](https://doi.org/10.1051/0004-6361/201219414)
- Tang, Y.-W., Guilloteau, S., Dutrey, A., et al. 2017, *ApJ*, 840, 32, doi: [10.3847/1538-4357/aa6af7](https://doi.org/10.3847/1538-4357/aa6af7)
- Teague, R. 2019, *The Journal of Open Source Software*, 4, 1632, doi: [10.21105/joss.01632](https://doi.org/10.21105/joss.01632)
- Teague, R. 2020, richteague/keplerian_mask: Initial Release, 1.0, Zenodo, doi: [10.5281/zenodo.4321137](https://doi.org/10.5281/zenodo.4321137)
- Teague, R., & Foreman-Mackey, D. 2018a, bettermoments: A robust method to measure line centroids, v1.0, Zenodo, doi: [10.5281/zenodo.1419754](https://doi.org/10.5281/zenodo.1419754)
- . 2018b, *Research Notes of the American Astronomical Society*, 2, 173, doi: [10.3847/2515-5172/aae265](https://doi.org/10.3847/2515-5172/aae265)
- Thieme, T. J., Lai, S.-P., Lin, S.-J., et al. 2022, *ApJ*, 925, 32, doi: [10.3847/1538-4357/ac382b](https://doi.org/10.3847/1538-4357/ac382b)
- Valdivia-Mena, M. T., Pineda, J. E., Segura-Cox, D. M., et al. 2022, *A&A*, 667, A12, doi: [10.1051/0004-6361/202243310](https://doi.org/10.1051/0004-6361/202243310)
- . 2023, *A&A*, 677, A92, doi: [10.1051/0004-6361/202346357](https://doi.org/10.1051/0004-6361/202346357)
- van der Marel, N., Birnstiel, T., Garufi, A., et al. 2021, *AJ*, 161, 33, doi: [10.3847/1538-3881/abc3ba](https://doi.org/10.3847/1538-3881/abc3ba)
- van der Velden, E. 2020, *The Journal of Open Source Software*, 5, 2004, doi: [10.21105/joss.02004](https://doi.org/10.21105/joss.02004)
- van Gelder, M. L., Tabone, B., van Dishoeck, E. F., & Godard, B. 2021, *A&A*, 653, A159, doi: [10.1051/0004-6361/202141591](https://doi.org/10.1051/0004-6361/202141591)
- Veronesi, B., Paneque-Carreño, T., Lodato, G., et al. 2021, *ApJL*, 914, L27, doi: [10.3847/2041-8213/abfe6a](https://doi.org/10.3847/2041-8213/abfe6a)
- Virtanen, P., Gommers, R., Oliphant, T. E., et al. 2020, *Nature Methods*, 17, 261, doi: [10.1038/s41592-019-0686-2](https://doi.org/10.1038/s41592-019-0686-2)
- Winter, A. J., Benisty, M., & Andrews, S. M. 2024, *ApJL*, 972, L9, doi: [10.3847/2041-8213/ad6d5d](https://doi.org/10.3847/2041-8213/ad6d5d)
- Zhou, Y., Sanghi, A., Bowler, B. P., et al. 2022, *ApJL*, 934, L13, doi: [10.3847/2041-8213/ac7fef](https://doi.org/10.3847/2041-8213/ac7fef)